JCB Journal of Cell Biology

ARTICLE

Rab18 regulates focal adhesion dynamics by interacting with kinectin-1 at the endoplasmic reticulum

Noemi Antonella Guadagno[1], Azzurra Margiotta[1], Synne Arstad Bjørnestad[1], Linda Hofstad Haugen[1], Ingrid Kjos[1], Xiaochun Xu[2], Xian Hu[1], Oddmund Bakke[1], Felix Margadant[2], and Cinzia Progida[1]

The members of the Rab family of small GTPases are molecular switches that regulate distinct steps in different membrane traffic pathways. In addition to this canonical function, Rabs can play a role in other processes, such as cell adhesion and motility. Here, we reveal the role of the small GTPase Rab18 as a positive regulator of directional migration in chemotaxis, and the underlying mechanism. We show that knockdown of Rab18 reduces the size of focal adhesions (FAs) and influences their dynamics. Furthermore, we found that Rab18, by directly interacting with the endoplasmic reticulum (ER)-resident protein kinectin-1, controls the anterograde kinesin-1–dependent transport of the ER required for the maturation of nascent FAs and protrusion orientation toward a chemoattractant. Altogether, our data support a model in which Rab18 regulates kinectin-1 transport toward the cell surface to form ER–FA contacts, thus promoting FA growth and cell migration during chemotaxis.

Introduction

Rab proteins constitute the largest family within the Ras superfamily of small GTPases. The first Rabs were identified in yeast in the 1980s (Gallwitz et al., 1983; Schmitt et al., 1986), and today >60 members have been revealed in humans (Zhen and Stenmark, 2015). Rab proteins are master regulators of intracellular membrane traffic, and by localizing to different membrane compartments, they control the specificity of vesicular transport and ensure that the cargoes are transported to their correct destinations within the cell (Wandinger-Ness and Zerial, 2014; Zhen and Stenmark, 2015). Rabs function as molecular switches that alternate between an active GTP-bound state and an inactive GDP-bound state. Upon membrane recruitment, Rab proteins in their GTP-bound state can bind a variety of different effector molecules, including sorting adaptors, tethering factors, fusion regulators, kinases, phosphatases, and motor proteins (Gillingham et al., 2014).

More recently, Rab proteins have been shown to take part in other cellular processes. These small GTPases can indeed regulate the mitotic spindle and abscission during cell division (Gibieža and Prekeris, 2018; Kouranti et al., 2006), apical lumen formation and polarization of epithelial cells (Bryant et al., 2010), nutrient sensing, and signaling (Thomas et al., 2014). Interestingly, an increasing amount of evidence shows that Rab proteins are implicated in the processes of cell migration and invasion (Borg et al., 2014; Linford et al., 2012; Palamidessi et al., 2008; Vestre et al., 2019). This function is often connected to their role in mediating intracellular transport, but can also be associated with their ability to regulate cytoskeleton dynamics (Borg et al., 2014; Kjos et al., 2018; Lanzetti et al., 2004; Linford et al., 2012; Palamidessi et al., 2008). Indeed, Rab proteins can influence cytoskeleton dynamics, for example through cross-talk with Rho GTPases (Borg et al., 2014; Bravo-Cordero et al., 2016; Chevallier et al., 2009; Jian et al., 2016; Margiotta et al., 2017; Palamidessi et al., 2008; Vestre et al., 2019).

Rab18 is one of the most highly conserved Rab GTPases (Klöpper et al., 2012). It localizes to the ER and lipid droplets (LDs), and it has been described to regulate LD growth and maturation by establishing contacts between LDs and the ER (Li et al., 2019; Martin et al., 2005; Ozeki et al., 2005; Xu et al., 2018). Depletion of Rab18 causes defects in LD morphology but also in ER tubule integrity (Carpanini et al., 2014; Gerondopoulos et al., 2014; Jayson et al., 2018). Furthermore, Rab18 is also reported to regulate ER trafficking (Dejgaard et al., 2008), as well as secretory granule transport (Vazquez-Martinez et al., 2007).

[1]Department of Biosciences, University of Oslo, Oslo, Norway; [2]Mechanobiology Institute, National University of Singapore, Singapore.

Correspondence to Cinzia Progida: c.a.m.progida@ibv.uio.no; I. Kjos's current address is Institute for Cancer Research, Oslo University Hospital, Oslo, Norway.

Loss-of-function mutations in *Rab18* gene causing altered ER morphology have been identified in Warburg micro syndrome, a human neurological and developmental disorder in which Rab18 has a critical role as a regulator of neuronal migration and morphogenesis (Bem et al., 2011; Gerondopoulos et al., 2014; Wu et al., 2016). However, how the loss-of-function of a protein regulating ER trafficking and morphology results in defects of cell migration is poorly understood, which emphasizes the importance of further investigating the contribution of Rab18 to this process.

We therefore elucidate the role of Rab18 in cell migration and the underlying mechanism. In particular, we investigate whether this function is connected to kinectin-1 (KNT1) function. KNT1 is an integral transmembrane protein that connects the ER to the microtubule motor kinesin-1 (Ong et al., 2000). Evidence indicates that KNT1-kinesin interaction mediates the anterograde transport of the ER to support FA growth and maturation during cell migration, but what regulates the KNT1-kinesin–mediated transport of the ER to the leading edge remains unresolved (Ng et al., 2016; Zhang et al., 2010).

Here, we identify that Rab18 directly interacts with KNT1. Furthermore, we show that this interaction is required to mediate the anterograde ER transport to promote ER–FA contacts and thus, FA maturation. Indeed, impairment of Rab18 recruitment to KNT1 reproduces the previously described phenotype obtained upon KNT1 depletion with cells exhibiting defects in FA growth. Furthermore, Rab18 knockdown affects protrusion orientation toward a chemoattractant, suggesting that the interaction between Rab18 and KNT1, by promoting FA maturation, allows the maintenance of protrusion oriented toward the chemoattractant. Collectively, our work resolves the molecular dependencies between Rab18, KNT1 and kinesin-1 and identifies Rab18 as an activator of the kinesin-1-KNT1-anterograde ER transport required for proper FA maturation, protrusion orientation, and directional migration in chemotaxis.

Results

Rab18 directly interacts with KNT1

Rab18 is a small GTPase localized to the ER, where it is involved in the maintenance of the ER structure (Gerondopoulos et al., 2014), trafficking (Dejgaard et al., 2008), and formation of LD–ER contact required for LD growth (Li et al., 2019; Ozeki et al., 2005; Xu et al., 2018). Recently, it has been shown to also regulate neuronal migration and morphogenesis during development (Wu et al., 2016). However, as the molecular mechanisms used by Rab18 in cell migration are not fully elucidated, we aimed to characterize its role in this process. Interestingly, KNT1, an integral ER membrane protein that binds to the motor protein kinesin to mediate microtubule plus-end–directed transport, promotes the anterograde ER transport to support FA maturation during chemotaxis (Ng et al., 2016; Ong et al., 2000; Zhang et al., 2010). We therefore wondered whether the role of Rab18 in cell migration could be connected to KNT1 function. To answer this question, we first analyzed the intracellular localization of both Rab18 and KNT1. U2OS cells transfected with GFP-Rab18 were fixed and immunostained using an antibody directed against KNT1. Confocal microscopy analysis showed that the two proteins indeed colocalize at the ER and in proximity to the plasma membrane, where they also overlap with the FA protein vinculin (Fig. 1 a). Therefore, we next investigated whether Rab18 interacts with KNT1. For this, we performed coimmunoprecipitation (coIP) experiments in U2OS cells transiently transfected with GFP, GFP-Rab18 WT, the constitutively active mutant GFP-Rab18 Q67L, or the dominant-negative mutant GFP-Rab18 S22N. Both Rab18 WT and Q67L were able to immunoprecipitate KNT1 (Fig. 1 b), indicating that KNT1 is a Rab18 effector.

To gain more insight into the interaction between Rab18 and KNT1, we mapped the Rab18-binding region on KNT1 using a series of deletion mutants of KNT1 (Fig. 1 c). CoIP results demonstrated that Rab18 binds to the transmebrane (TM) mutant containing the first 445 amino acids of KNT1, including the transmembrane domain responsible for the insertion of KNT1 into the ER membrane and a portion of the cytoplasmic domain (Fig. 1, c and d; Abe et al., 2007; Fütterer et al., 1995; Santama et al., 2004; Yu et al., 1995). To further restrict the Rab18-binding domain on KNT1, we designed an additional mutant of KNT1, KNT1 Δ201–445. This mutant contains the N-terminus region responsible for the insertion into the ER membrane as well as the C-terminus coiled-coil cytoplasmic region responsible for KIF5B binding (Ong et al., 2000), but lacks residues 201–445 of the cytoplasmic region, which are instead present in the TM mutant (Fig. 1, c–e). CoIP experiments demonstrated that KNT1 Δ201–445 is not able to bind to Rab18 (Fig. 1 e), thus indicating that the Rab18-binding domain on KNT1 is within the cytoplasmic region between residues 200 and 445.

We next investigated whether Rab18 and KNT1 interact directly. Purified bacterially expressed GST-tagged KNT1 (residues 201–445) was incubated together with purified His-tagged Rab18 Q67L, and then GST-tagged KNT1 (201–445) was precipitated using glutathione resin. Western blot analysis of the precipitated proteins revealed that Rab18 is able to specifically bind to GST-KNT1 (201–445), and that no binding of Rab18 to GST protein alone was detected (Fig. 1 f), demonstrating that Rab18 directly interacts with KNT1.

Rab18 and KNT1 form a complex together with kinesin-1 to mediate ER anterograde transport to FA sites

The discovery of the interaction between Rab18 and KNT1 suggests that this complex might regulate the KNT1 plus-end–mediated transport of the ER (Zhang et al., 2010). To further investigate this hypothesis, we analyzed the localization of KNT1 by immunofluorescence on either control or Rab18 knockdown cells. As shown in Fig. 2, a and b, the silencing of Rab18 induced KNT1 accumulation in the perinuclear area. Indeed, compared with the control cells, in which 35% of the total KNT1 was present in the perinuclear region, in Rab18 knockdown cells, almost 60% of the total KNT1 was localized in the perinuclear area. The reintroduction of Rab18 in knockdown cells rescued the localization defect, indicating that Rab18 is indeed involved in KNT1-mediated transport.

KNT1 binds kinesin-1 heavy chain (KIF5B) to mediate microtubule plus-end–directed transport (Kumar et al., 1995; Ong

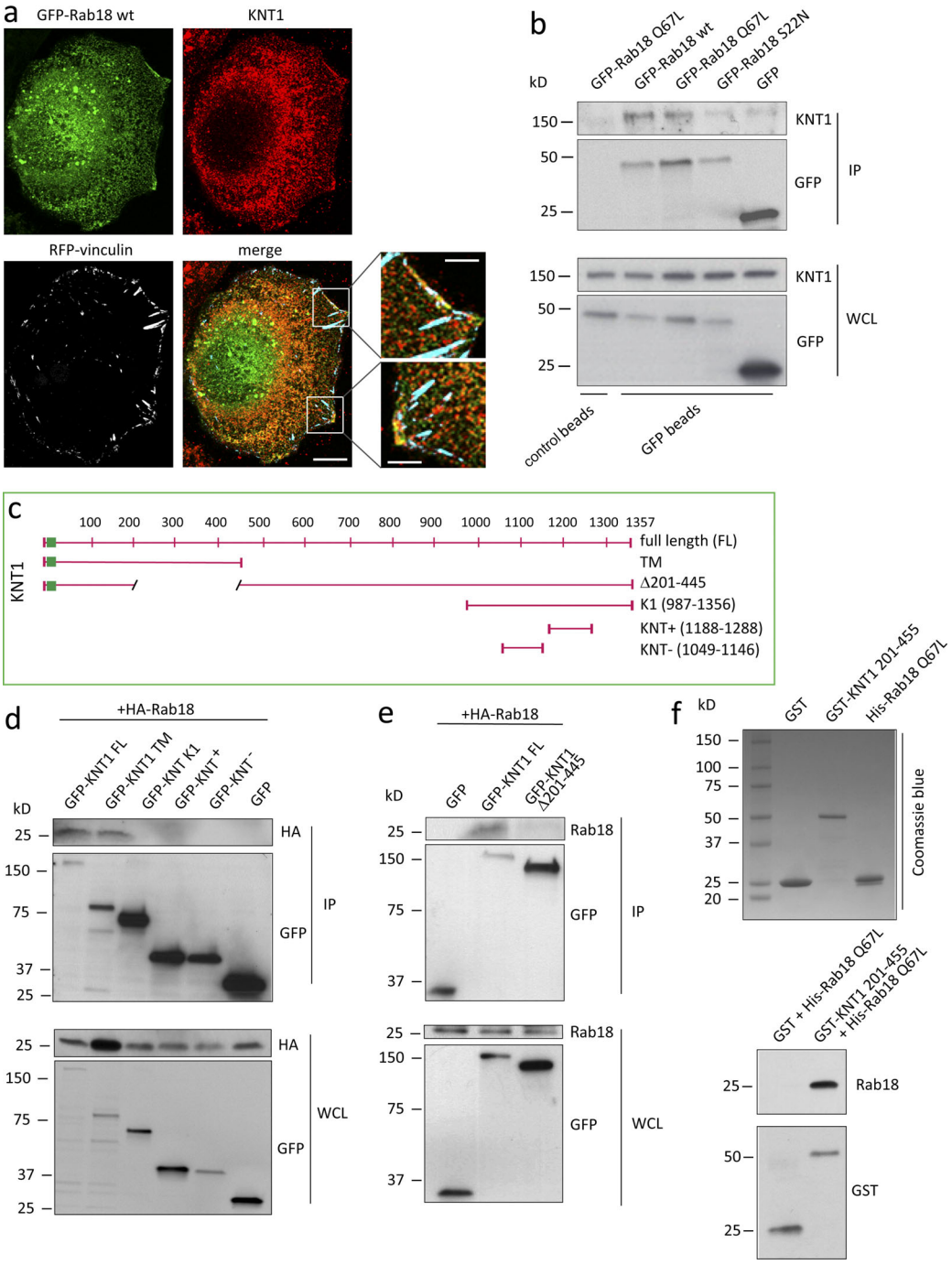

Figure 1. **Rab18 directly interacts with KNT1. (a)** Representative image of a cell transfected with GFP-Rab18 WT and RFP-vinculin and immunostained with an antibody against KNT1. The insets show regions (white squares) where GFP-Rab18 and KNT1 colocalize in proximity of the plasma membrane with the FA protein vinculin (cyan). Scale bar: 10 µm; insets: 1 µm. **(b)** U2OS cells were transiently transfected with GFP, GFP-Rab18 WT, GFP-Rab18 Q67L, or GFP-Rab18 S22N, lysed, and subjected to IP with GFP or control magnetic agarose beads. Whole-cell lysates (WCL) and immunoprecipitates (IP) were subjected to Western blot analysis using the indicated antibodies. **(c)** Schematic representation of KNT1 FL and deletion mutants used in this study. The green square indicates the ER membrane-binding domain of KNT1. **(d)** U2OS cells were transiently cotransfected with HA-Rab18 and GFP, GFP-KNT1 FL, TM, K1, KNT$^+$, or KNT$^-$, lysed, and immunoprecipitated with GFP magnetic agarose beads. WCL and IP were subjected to Western blot analysis using the indicated antibodies. **(e)** U2OS cells were transiently cotransfected with HA-Rab18 and GFP, GFP-KNT1 FL, or Δ201–445, lysed, and immunoprecipitated with GFP magnetic agarose beads. WCL and IP were subjected to Western blot analysis using the indicated antibodies. **(f)** Top: Coomassie blue staining of bacterially expressed and purified GST, GST-KNT1 (201–445), and His-Rab18 Q67L. Bottom: Purified GST or GST-KNT1 (201–445) was incubated with purified His-Rab18 Q67L. Samples were subjected to affinity chromatography followed by Western blot analysis using antibodies specific to GST and Rab18.

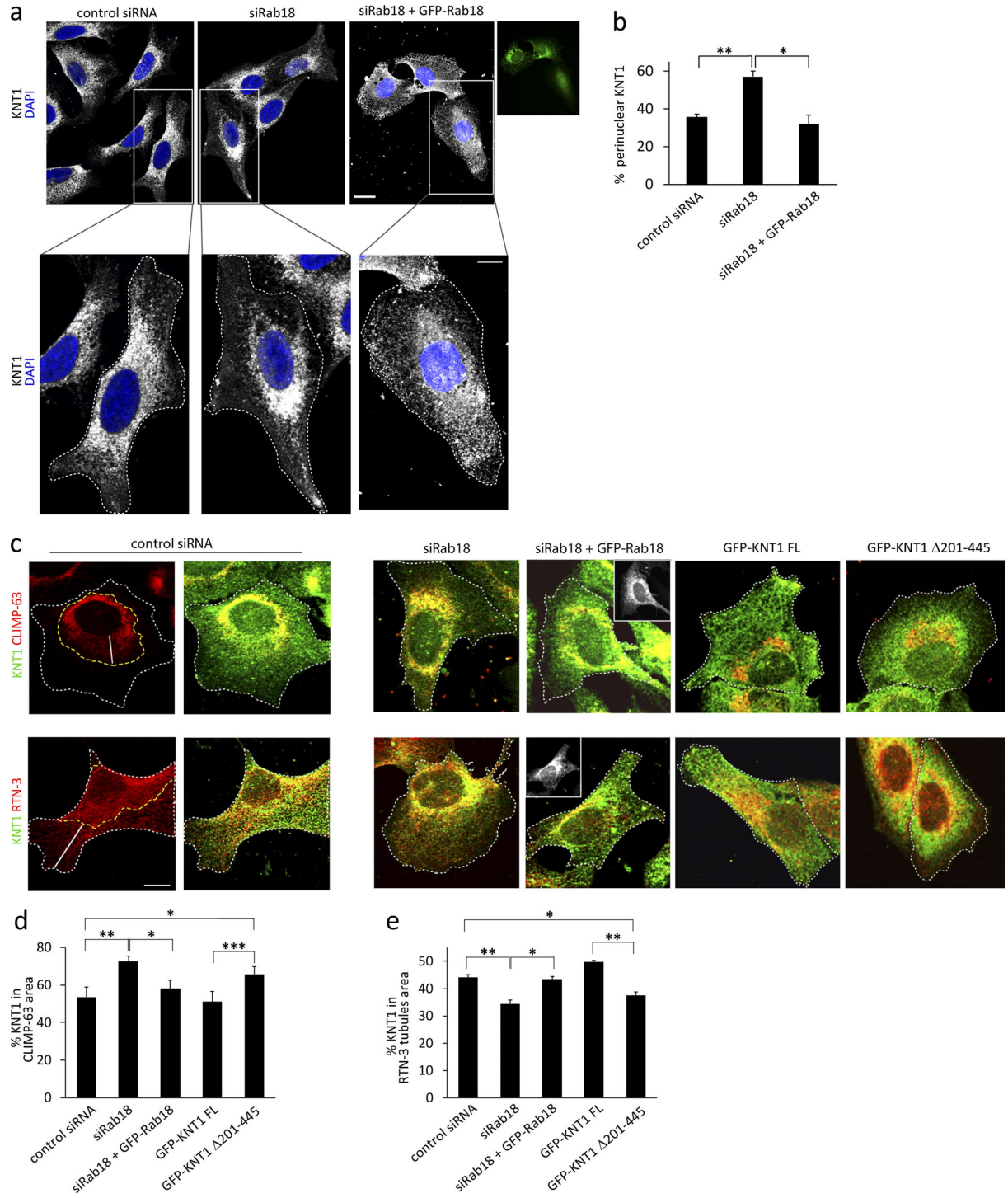

Figure 2. **Rab18 binding is required for KNT1 localization at the peripheral tubular ER. (a)** U2OS cells transfected with siRNA control or siRNA against Rab18, or depleted for Rab18 and subsequently transfected with GFP-Rab18, were fixed and stained with DAPI and anti-KNT1 antibody. The insets show magnifications of the boxed areas and illustrate examples of KNT1 distribution under the different conditions. The inset shows the GFP channel for the sample transfected with GFP-Rab18. Images represent maximum-intensity projections from Z-stacks. Scale bar: 20 µm; inset: 10 µm. **(b)** Quantification of KNT1 intracellular distribution in control cells, cells knocked down for Rab18, and cells knocked down for Rab18 and transfected with GFP-Rab18. The graph represents the percentage of perinuclear KNT1 over the total. Data represent the mean ± SEM of three independent experiments (n > 60). *, P < 0.05; **, P < 0.01. **(c)** U2OS cells were transfected with control siRNA, siRNA against Rab18, or siRNA depleted for Rab18 and subsequently transfected with GFP-Rab18 or stably transfected with GFP-KNT1 FL or GFP-KNT1 Δ201–445. Cells were fixed and stained with anti-KNT1 and CLIMP-63 or RTN-3 antibody. Left: ER sheets area labeled by CLIMP-63 (top) and ER tubular area labeled by RTN-3 (bottom). Insets: GFP channel for the cells transfected with GFP-Rab18. Scale bar: 10 µm. **(d and e)** Quantification of KNT1 intracellular distribution in sheet (CLIMP-63; d) and tubule (RTN-3; e) area over the total. Data represent the mean ± SEM of three independent experiments (n > 60). *, P < 0.05; **, P < 0.01; ***, P < 0.001.

et al., 2000; Toyoshima et al., 1992; Zhang et al., 2010). We therefore wondered whether Rab18 is part of this KNT1 and KIF5B complex. CoIP experiments in U2OS cells transiently transfected with either GFP or GFP-Rab18 WT showed that Rab18 immunoprecipitates endogenous KIF5B (Fig. S1 a). However, KNT1 knockdown prevents the binding of KIF5B to Rab18, suggesting that KNT1 is an adaptor that bridges Rab18 to KIF5B (Fig. S1 a). In line with this model, silencing of Rab18 did not affect the interaction between KNT1 and KIF5B (Fig. S1 b).

To further assess the role of Rab18 binding to KNT1 in KNT1 distribution within the ER and in KIF5B-mediated transport, we compared KNT1 localization in ER sheet and tubule compartments in cells depleted for Rab18 or expressing the KNT1 Δ201–445 mutant defective for Rab18 binding, using CLIMP-63 and reticulon 3 as markers of these compartments. KNT1 redistributes to ER sheets both in cells silenced for Rab18 and in cells stably expressing KNT1 Δ201–445 (Fig. 2, c–e). This further supports the role of Rab18 binding in promoting KNT1-anterograde transport toward the peripheral tubular ER and indicates that the binding of KNT1 to KIF5B is not sufficient to mediate this transport in the absence of Rab18.

KNT1 mediates the anterograde transport of the ER to support FA growth and maturation (Zhang et al., 2010). To further explore whether this process is dependent on the interaction with Rab18, we analyzed the ER–FA contacts in cells silenced for Rab18 and cotransfected with ER-GFP and RFP-vinculin. The results indeed showed a reduction in the contact points between ER and FAs of ∼20% when Rab18 was knocked down (Fig. 3, a and b), supporting the role of Rab18 in KNT1-mediated ER transport toward the surface to promote FA growth. Moreover, live imaging analysis of cells spreading on fibronectin-coated dishes revealed that silencing of Rab18 indeed delays the formation of contacts between the ER and FAs, and that the re-expression of Rab18 in these cells restores not only the time required for contact establishment but also the percentage of FAs in contact with the ER (Fig. S2, a–c).

For a functional evaluation of the role of the Rab18–KNT1 interaction in mediating the transport of the ER toward FAs, we performed loss-of-function and rescue experiments with KNT1 mutants defective in the interaction with either Rab18 or KIF5B. U2OS cells silenced for KNT1 were transfected with dsRed-ER alone or cotransfected with dsRed-ER and GFP-KNT1 full length (FL), TM, or Δ201–445, fixed, and immunostained using an antibody directed against vinculin. Confocal microscopy analysis showed a reduction in the contact points between ER and FAs of ∼40% when KNT1 was knocked down, compared with the control siRNA. Only the expression of GFP-KNT1 FL rescued the defect in ER–FA contacts, while KNT1 mutants defective in the interaction with either KIF5B (KNT1 TM) or Rab18 (KNT1 Δ201–445) were not able to rescue the ER-transport defects (Fig. 3, c and d). This demonstrates that the binding of both Rab18 and KIF5B to KNT1 is required for the correct transport of the ER toward the cell surface to establish contacts with FAs.

Rab18 influences FA size and traction force generation

KNT1-mediated ER transport to the cell periphery is required to support FA growth (Zhang et al., 2010). We therefore wondered whether the interaction between Rab18 and KNT1 is involved in the regulation of FAs. To test this hypothesis, we analyzed FA size and number in cells silenced for Rab18. Control cells and cells silenced for Rab18 were fixed and stained with rhodamine-phalloidin and an antibody against vinculin to label actin fibers and FAs, respectively. Quantification of FA size showed an ∼30% decrease in FA size in cells silenced for Rab18, as well as a decrease in the total number of FAs, which were both at least partially restored after the reintroduction of Rab18 in the cells (Fig. 4, a–c). The number of FAs per cell area, however, was not significantly affected (Fig. 4 d). Therefore, these results suggest that FAs are still formed in absence of Rab18, and that their reduced size may be rather caused by defects in a later stage during the maturation process. Cells stably expressing the KNT1 Δ201–445 mutant defective in the binding to Rab18 recapitulated the same defects in FAs observed upon Rab18 depletion (Fig. 4), indicating that Rab18-binding to KNT1 is required for FA growth.

The decrease in total number of FAs but not in the number of FAs per cell area in cells silenced for Rab18 suggests a defect in cell spreading upon Rab18 knockdown. Therefore, we investigated whether Rab18 depletion inhibits cell spreading by using two different siRNAs targeting Rab18 (siRab18 and siRab18_1). The average area of control cells seeded and allowed to adhere on fibronectin-coated coverslips for 1 h was ∼500 µm^2, whereas the area of cells silenced for Rab18 was <300 µm^2, showing a significant reduction in cell spreading by ∼50% for both siRNAs. Moreover, expression of GFP-Rab18 in cells silenced for Rab18 rescued the spreading defect (Fig. 5, a–c).

To further dissect the role of Rab18 in cell spreading, we plated cells on adhesive micropatterned surfaces. These tools allow normalization of the shape and internal polarity of each cell, overcoming the variability in cell morphology that typically occurs in cells plated on regular culture dishes. Such normalization of the intracellular architecture facilitates quantification of even small effects on the actin cytoskeleton (Degot et al., 2010). Hence, we used L-shaped fibronectin-coated micropatterns to investigate whether Rab18 influences the organization of actin cytoskeleton during cell adhesion and spreading (Fig. 5, d–f). On these patterns, the cells normally adhere on the adhesive L-shaped sides and spread, generating a right-angled triangle with a straight hypotenuse made by stress fibers, which are more pronounced above nonadhesive edges (Degot et al., 2010; Théry, 2010). We calculated the ability of control cells or cells knocked down for Rab18 to normally spread and stretch on L-patterns by comparing the number of cells that were straight (fully spread and stretched) and curved (unspread or collapsed along the hypotenuse; Fig. S3, a and b). As expected, the majority of the control cells (almost 90%) were able to fully spread and form stress fibers along the hypotenuse. Interestingly, a decrease in the number of fully spread cells of ∼50% for the cells silenced with siRab18_1 and ≤70% for the cells silenced with siRab18, and a consequent increase in the number of cells defined as curved, was observed upon Rab18 silencing (Fig. 5, d and e). This increase includes both the cells collapsed along the hypotenuse and the cells unable to fully spread on the micropattern (Fig. S3 b).

To further investigate the distribution of the actin cytoskeleton in cells silenced for Rab18, we used an algorithm that aligns

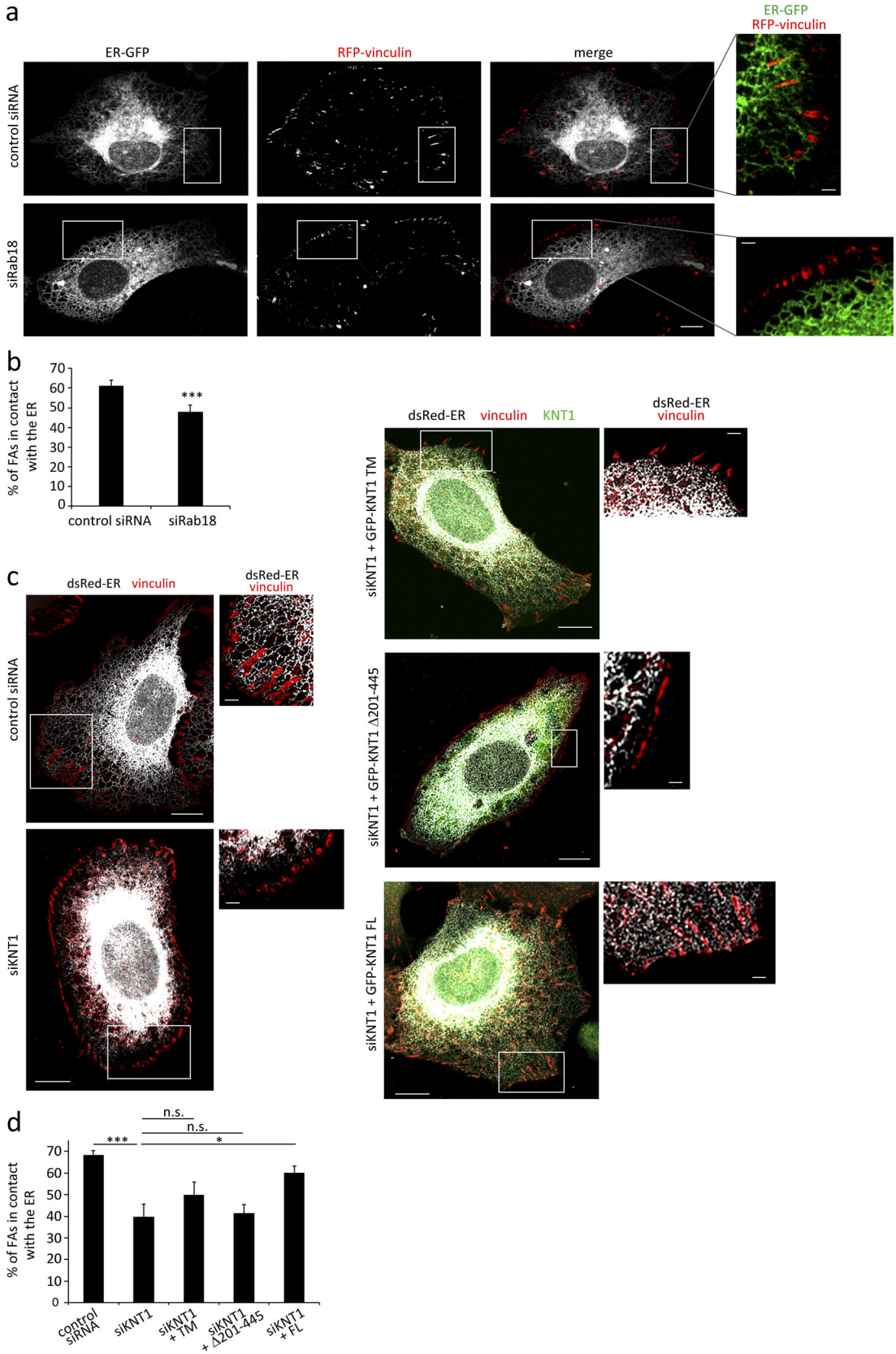

Figure 3. **Formation of ER–FA contacts is dependent on the binding of Rab18 and KIF5B to KNT1. (a)** U2OS cells silenced with siRNA control or siRNA targeting Rab18 were cotransfected with ER-GFP and RFP-vinculin. The images represent maximum-intensity projections from Z-stacks. The insets show magnifications of the boxed regions. Scale bar: 10 µm; insets: 2 µm. **(b)** Quantification of the percentage of FAs in contact with the ER. The graph represents the mean ± SEM from three independent experiments (n > 30 cells). ***, P < 0.001. **(c)** U2OS cells were treated with either control siRNA or siRNA directed

against KNT1 and transfected with either dsRed-ER alone or together with either GFP KNT1 FL, TM, or Δ201–445. Cells were fixed and stained with anti-vinculin antibody. The images represent maximum-intensity projections from Z-stacks. The insets show magnification of boxed regions to illustrate contact points between ER and FAs. Scale bars: 10 µm; insets: 2 µm. **(d)** Quantification of the percentage of FAs in contact with the ER. The graph represents the mean ± SEM from three independent experiments (n > 30 cells). *, P < 0.05; ***, P ≤ 0.001; n.s., not significant.

and averages several micropatterned cells, generating a color-coded frequency map (Degot et al., 2010). Consistent with the previous results, the analysis revealed that the intensity of the actin along the hypotenuse is weaker upon Rab18 silencing, indicating a reduction of the actin fibers along the hypotenuse (Fig. 5 f).

Cells form stress fibers between adhesion sites, which promote the production of traction forces (Bershadsky et al., 2003; Livne and Geiger, 2016). On micropatterns, the generation of the force occurs along the hypotenuse (Théry, 2010). We therefore hypothesized that, given their alterations in actin stress fibers, Rab18-depleted cells are not able to generate the traction forces necessary to translocate their cell bodies. To test this, we used microfabricated PMDS pillars. These elastic micropillars function as force sensors, as their deflection is directly proportional to the force generated by the cell in the planar direction (Balaban et al., 2001; Schoen et al., 2010). We seeded control cells and cells knocked down for Rab18 on fibronectin-coated PMDS micropillars for 2 h and measured the force applied by the cells on the substrate. The results showed that the cells silenced for Rab18 applied a smaller force on the substrate at the initial time points (Fig. S3, c and d), which is consistent with the defective spreading and actin stress fibers observed upon Rab18 knockdown.

Rab18 is required for the maturation of FAs

Live imaging analysis of cells transfected with GFP-Rab18 and RFP-vinculin revealed a correlation between the fluorescent intensity of the two proteins over time in regions of FA assembly or disassembly, with both Rab18 and vinculin intensities increasing during FA assembly or decreasing during FA disassembly (Fig. S4 and Video 1). This, together with the role of Rab18 in the transport of the ER to FAs, suggests a possible involvement of this small GTPase in the control of FA dynamics and growth.

To further understand the role of Rab18 in FA turnover, we transfected with RFP-vinculin the cells silenced with either control siRNA or siRab18 and monitored FA assembly and disassembly in live cells (Fig. 6, a and b). FA assembly and disassembly rates were calculated as the percentage of FAs that assembled or disassembled per minute. In agreement with the data on FA size, FA dynamics were affected by the knockdown of Rab18. Indeed, the assembly rate was ∼2.4-fold lower in silenced cells compared with controls, while the disassembly rate was threefold higher, strongly supporting a role for Rab18 in FA turnover (Fig. 6 c). Moreover, the KNT1 mutants K1 and Δ201–445, which are both defective in Rab18 binding, show more similar defects in FA turnover than upon Rab18 depletion (Fig. 6, b and c), indicating that the binding of Rab18 to KNT1 is required for the regulation of FA dynamics.

FAs are initiated by activation of integrins. Upon ligand binding, integrins recruit additional proteins to their cytoplasmic tails, including vinculin, paxillin and FA kinase (FAK), resulting in the maturation of the adhesions (Humphries et al., 2007; Sun et al., 2016; Zaidel-Bar et al., 2003). To finally assess whether the Rab18- and KNT1-mediated transport of the ER toward the cell membrane facilitates the recruitment of FA proteins, such as β3-integrins and then vinculin, to support FA growth and maturation, we performed FRAP experiments. U2OS cells were cotransfected with DsRed-ER and either β3-integrin-YFP or vinculin-GFP, or with RFP-Rab18 and either β3-integrin-YFP or vinculin-GFP, and FAs with or without ER contact were photobleached (Fig. 7, a–c). FRAP analysis showed that for FAs in contact with the ER, silencing of Rab18 reduced the fluorescence recovery and the mobile fraction (MF) for both β3-integrins and vinculin (Fig. 7 b). Expression of RFP-Rab18 in silenced cells restored the fluorescence recovery and the MFs for both FA proteins (Fig. 7 b). When FAs not contacting the ER were bleached, the fluorescence recovery was strongly reduced in all the samples, with comparable low MFs in both control cells and cell silenced for Rab18 (Fig. 7 c). Intriguingly, these MF values were similar to those measured for FAs in contact with the ER in cells silenced for Rab18, further supporting the role of this small GTPase in establishing the ER–FA contacts necessary to recruit FA proteins and support FA growth.

Integrin-mediated adhesion induces the autophosphorylation of FAK at Tyr-397, thereby maximizing its kinase activity and creating additional protein-binding sites (Mitra and Schlaepfer, 2006; Shi and Boettiger, 2003). FAK is also responsible for the phosphorylation of another FA protein, paxillin, which in turn recruits vinculin at the FAs (Case et al., 2015; Pasapera et al., 2010). Phosphorylation of FAK at Tyr-397 is also important for the control of FA turnover and disassembly (Hamadi et al., 2005; Webb et al., 2004). As our data demonstrate that Rab18 depletion influences FA maturation and dynamics, we wondered whether it also affects the phosphorylation of FAK on Tyr-397. Intriguingly, FAK phosphorylation decreased in cells knocked down for Rab18 compared with control cells (Fig. 7, d–g). Expression of GFP-Rab18 in silenced cells rescued the phosphorylation defect (Fig. 7, d–g), thus validating the specificity of the effect on FAK phosphorylation upon Rab18 depletion. Altogether, these results suggest a mechanism in which Rab18, by promoting the KNT1-mediated ER transport to FA sites, stimulates FA maturation through the recruitment of FA proteins and FAK activation.

Rab18 is required for cellular orientation during chemotaxis

KNT1 mediates ER transport preferentially to protrusions oriented toward a chemoattractant (Ng et al., 2016). To evaluate the contribution of Rab18 to this process, MDA-MB-231 cells were silenced for Rab18, and the orientation toward a chemoattractant (FCS) was quantified. Similarly to KNT1 silencing (Ng et al., 2016), Rab18 depletion also impaired directional bias of migration toward the chemoattractant. A Rayleigh test confirmed that

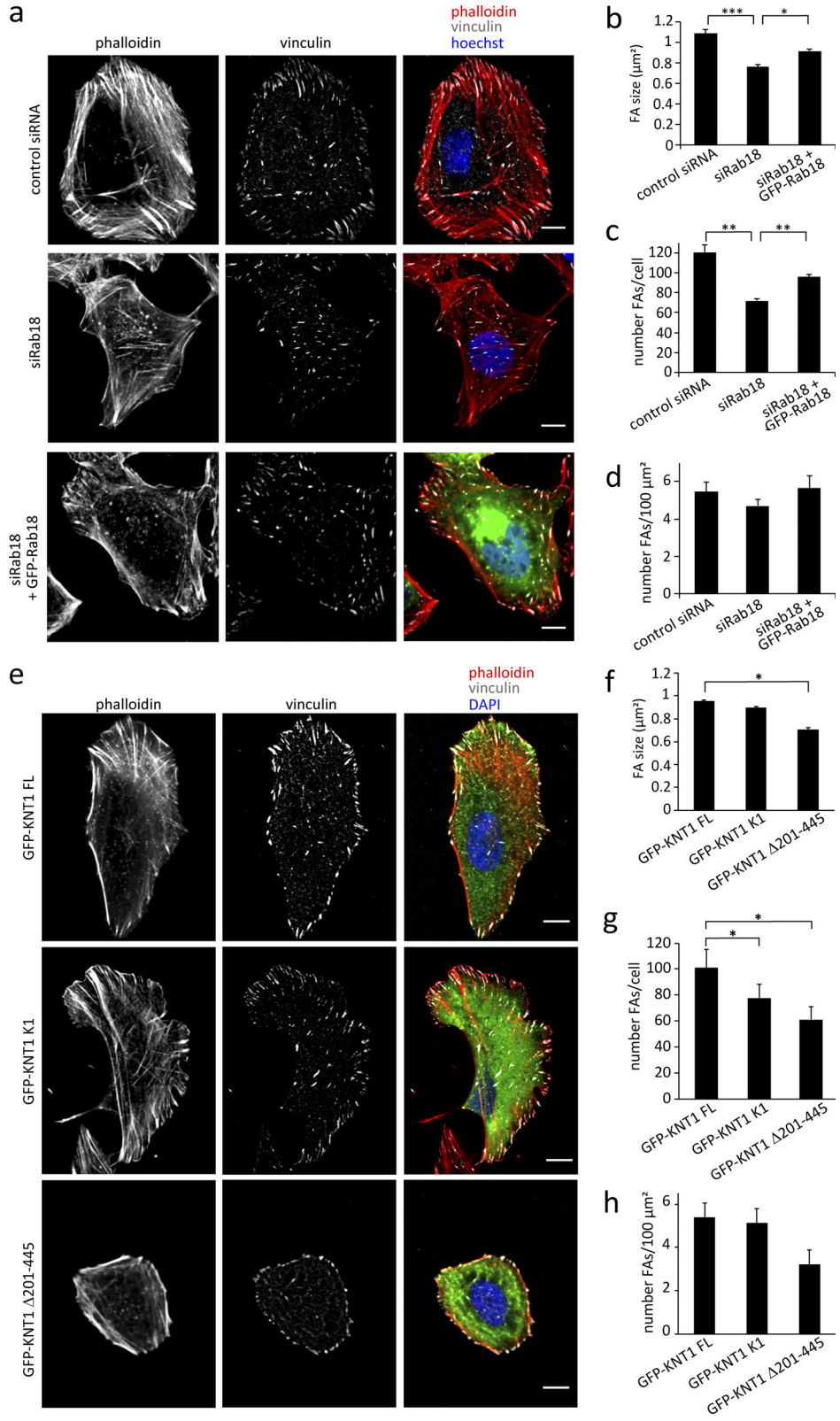

Figure 4. **Rab18-KNT1 interaction regulates FA size. (a)** U2OS cells silenced with siRNA control, siRNA against Rab18, or silenced with siRNA against Rab18 and subsequently transfected with GFP-Rab18 were fixed and stained with Hoechst, rhodamine-conjugated phalloidin, and an antibody against vinculin. Scale bar: 10 µm. **(b–d)** Quantification of the size (b) and number of FAs per cell (c) or per 100 µm² cell area (d). The graphs represent the mean ± SEM for three independent experiments (n > 120 cells) *, P < 0.05; **, P < 0.01; ***, P < 0.001. **(e)** U2OS cells stably transfected with GFP-KNT1 FL, K1, or Δ201–445 were fixed and stained with DAPI, rhodamine-conjugated phalloidin, and an antibody against vinculin. Scale bar: 10 µm. **(f–h)** Quantification of the size (f) and number of FAs per cell (g) or per 100 µm² cell area (h). The graphs represent the mean ± SEM for three independent experiments (n > 90 cells). *, P < 0.05.

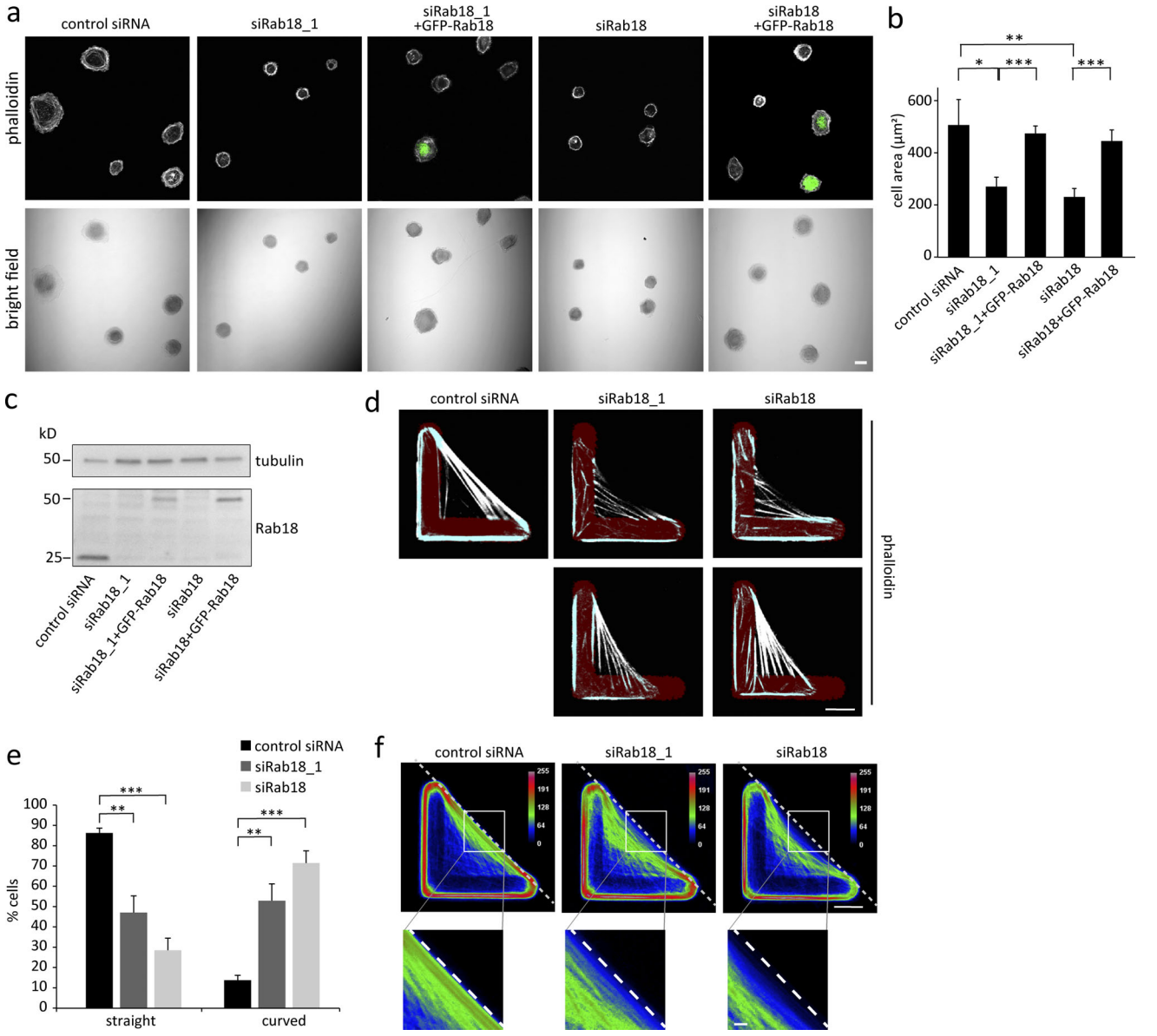

Figure 5. **Depletion of Rab18 affects cell spreading and architecture on adhesive micropatterns**. **(a)** U2OS cells transfected with siRNA control, siRNA Rab18, or siRNA Rab18_1, or treated with the same siRNAs against Rab18 and afterward transfected with GFP-Rab18, were plated on fibronectin-coated coverslips and left to adhere for 1 h before fixation and staining with rhodamine-conjugated phalloidin. Transmission images are shown in the lower panel. Scale bar: 20 µm. **(b)** Quantification of the average area. The graph represents the mean ± SEM; *n* > 80 cells per experiment for three independent experiments; *, P < 0.05; **, P < 0.01; ***, P < 0.001. **(c)** Cell lysates from control cells, cells silenced for Rab18, and cells silenced for Rab18 and transfected with GFP-Rab18 were subjected to Western blot analysis with antibodies against Rab18 and tubulin (as loading control). **(d)** U2OS cells treated with siRNA control, siRNA Rab18, or siRNA Rab18_1 were plated onto fibronectin-coated L-shaped micropatterns and left to adhere for 3.5 h before fixation and staining with rhodamine-conjugated phalloidin. The cells silenced for Rab18 show two different phenotypes: collapsed along the hypotenuse (top) or unable to fully spread on the micropattern (lower). The L-shaped micropattern is shown in red. Scale bar: 10 µm. **(e)** The percentage of cells with straight or curved hypotenuse (mean ± SEM). *n* > 80 cells from three independent experiments. **, P < 0.01; ***, P < 0.001. **(f)** Color-coded map of the actin distribution. The images were obtained by using the CellRef macro on averaged Z-projection images from aligned single stacks. Scale bar: 10 µm.

the distribution of migration direction was biased in the control but not in the Rab18-silenced cells, and that the reexpression of Rab18 rescued this defect (Fig. 8 a). The forward migration index in the y-direction was also decreased in the Rab18-depleted cells compared with the control cells or the cells reexpressing Rab18, further showing that knockdown of Rab18 results in the loss of preferential orientation toward the chemoattractant (Fig. 8 b). Moreover, while the majority of control cells extended a single protrusion toward the chemoattractant, cells depleted for Rab18 exhibited multiple and randomly oriented protrusions (Fig. 8, c and d). These results indicate that Rab18 contributes to directional migration toward the chemoattractant during chemotaxis and suggest that, similarly to KNT1, Rab18 is involved in the maintenance of cell protrusions oriented toward the chemoattractant by promoting FA maturation.

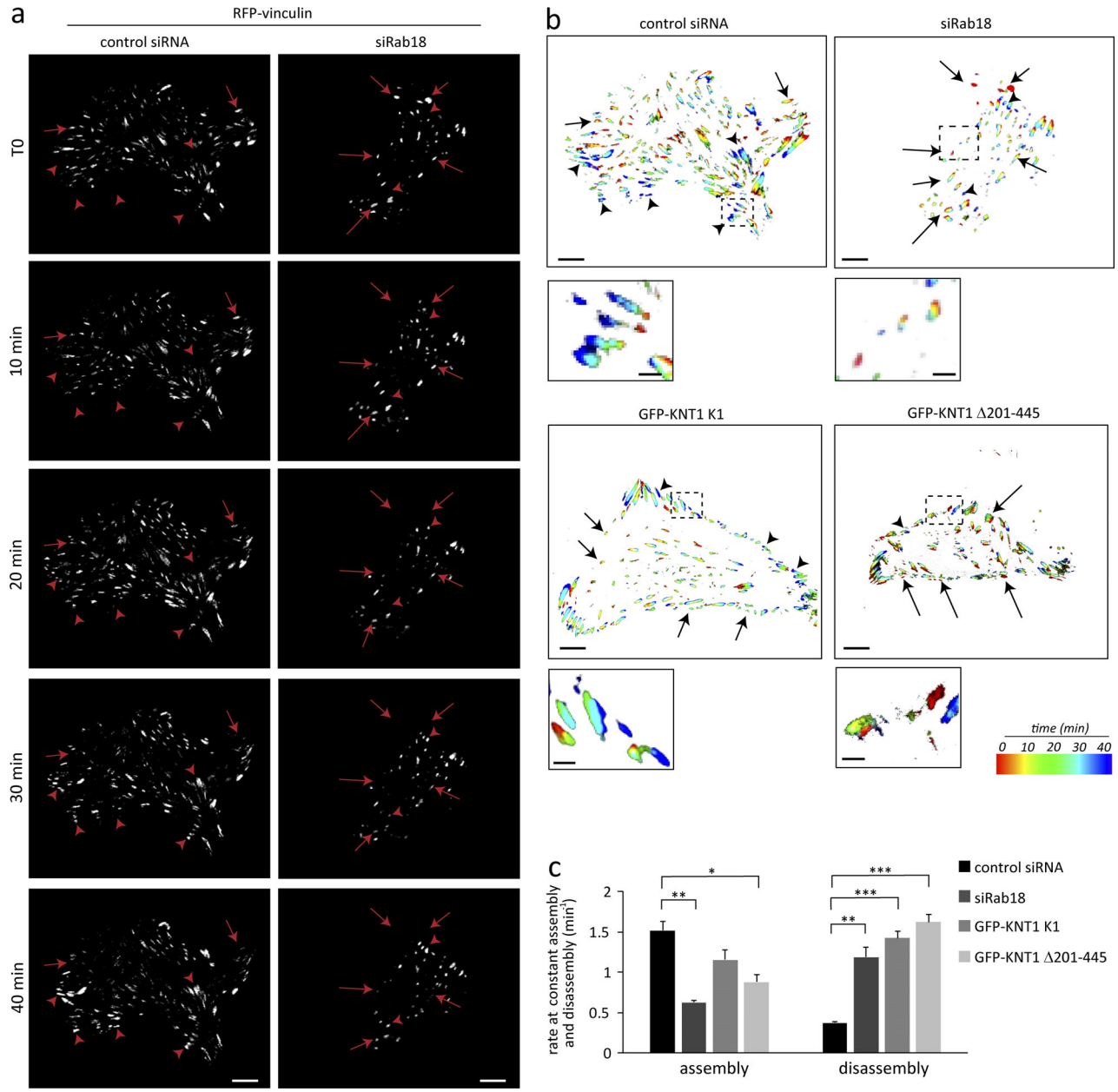

Figure 6. **Impaired binding of Rab18 to KNT1 affects FA assembly and disassembly rate. (a)** Control or Rab18-depleted cells transfected with RFP-vinculin were imaged every 10 min for 40 min. Arrows show FA disassembly, and arrowheads show FA assembly. Scale bar: 10 µm. **(b)** Rainbow color representation of FA appearance and disappearance over time from cells shown in panel a and for U2OS cells stably expressing GFP-KNT1 K1 or Δ201–445. Each time point is shown in a different color, as indicated in the bar. Insets show magnifications of the boxed areas. Scale bars: 10 µm; insets: 2 µm. **(c)** Quantification of assembly and disassembly rates of FAs. The assembly and disassembly rate is expressed as percentage of focal adhesion formation or disassembly per minute. The values represent the mean ± SEM from three independent experiments, in which 15 FAs were analyzed per cell (n > 6), per condition, and per experiment. *, P < 0.05; **, P < 0.01; ***, P < 0.001.

Discussion

Rab proteins are key regulators of intracellular membrane transport; however, they have been reported to play important roles in other cellular processes as well, including cell migration (Borg et al., 2014; Jian et al., 2016; Margiotta et al., 2017; Palamidessi et al., 2008; Vestre et al., 2019). In this study, we investigated the role of Rab18 in FA dynamics and directional migration during chemotaxis. This small GTPase has been recently shown to control neurite growth and neuronal migration during development in mice (Wu et al., 2016). However, the underlying mechanisms and whether this is a process regulated by Rab18 specifically only in neurons remain elusive. Here, we demonstrated that silencing of Rab18 impairs cellular orientation and directional migration during chemotaxis in human cancer cell lines, suggesting that this is a more general function regulated by Rab18.

Rab18 is localized to the ER, where it is involved in the maintenance of ER morphology and structure (Gerondopoulos

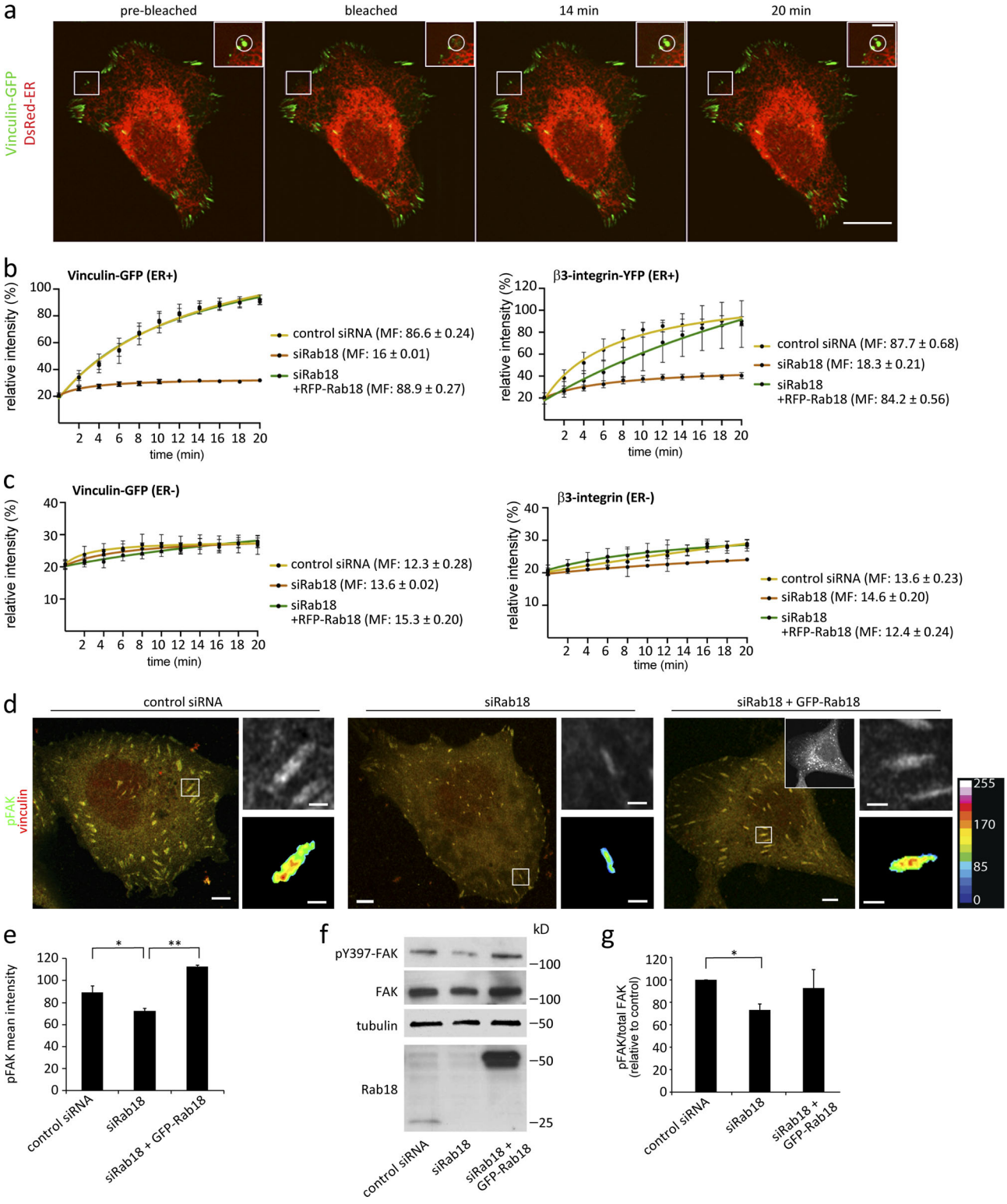

Figure 7. **Rab18 influences FA maturation and FAK phosphorylation. (a)** U2OS cells cotransfected with Vinculin-GFP and DsRed-ER imaged before (prebleach), during bleaching, and after photobleaching of one adhesion positive for Vinculin-GFP (white circle). Scale bar: 20 µm; inset: 4 µm. **(b and c)** Total linear fitted recovery curves with standard derivation for Vinculin-GFP or β3-integrin-YFP in control cells, cells silenced for Rab18, or cells silenced for Rab18 and transfected with RFP-Rab18. Curves show the recovery for adhesion points in contact with the ER (ER^+; b) or not (ER^-; c). For each curve, the value of the MF ± SEM is reported as percentage. A total of 27 adhesion points were bleached for each condition, in three independent experiments. **(d)** U2OS cells transfected with siRNA control or siRNA against Rab18, or depleted for Rab18 and subsequently transfected with GFP-Rab18, were fixed and stained with anti-pY397-FAK and anti-vinculin antibodies. Insets in the top right show magnifications of the boxed areas for pY397-FAK. Insets in the bottom right show the same adhesion with a color-coded map of the pY397-FAK mean fluorescence intensity. GFP channel for the cell silenced for Rab18 and transfected with GFP-Rab18 is shown in the upper right corner inset. Scale bar: 5 µm; inset: 1 µm. **(e)** Quantification of FAK activation on FAs measured as mean fluorescence intensity of

pY397-FAK per adhesion. The values represent the mean ± SEM of all the adhesions in a cell from three independent experiments (n > 30 cells). *, P < 0.05; **, P < 0.01. **(f)** Lysates from U2OS cells transfected with siRNA control, siRNA Rab18, or silenced for Rab18 and subsequently transfected with GFP-Rab18 were subjected to Western blot analysis with antibodies against FAK, pY397-FAK, Rab18, and tubulin (as loading control). **(g)** Quantification of FAK phosphorylation normalized to the levels of FAK and plotted relative to the control cells is shown as mean ± SEM from three independent experiments. *, P < 0.05.

et al., 2014), ER-Golgi trafficking (Dejgaard et al., 2008), regulation of secretory granules (Vazquez-Martinez et al., 2007), and formation of LD–ER contact required for LD growth (Li et al., 2019; Ozeki et al., 2005; Xu et al., 2018). How then could an ER-localized Rab regulate cell motility? Our data indicate that Rab18, by directly interacting with KNT1, mediates ER transport to FAs for the regulation of FA dynamics.

KNT1 is an integral ER membrane protein that serves as a receptor for the motor protein kinesin-1, thus mediating the anterograde movement of the ER on microtubules (Ong et al., 2000). KNT1 has a critical role in mediating ER transport to promote FA growth and maturation, as well as in correctly orienting and maintaining cell protrusions during chemotaxis (Ng et al., 2016; Zhang et al., 2010). It has been shown previously that overexpression of the minimal kinesin-1 interaction domain on KNT1 (KNT$^+$) causes defects in the number of FAs, cell spreading, migration, and ER extension into cellular lamella (Zhang et al., 2010), a phenotype similar to that we observed upon Rab18 depletion. This suggests that the binding of kinesin-1 to KNT1 is not sufficient to promote the KNT1-dependent movement of the ER toward the cell periphery and that other components are required to activate the complex. In line with this hypothesis, we revealed that Rab18 interacts with KNT1 and the kinesin-1 heavy chain, KIF5B (Figs. 1 and S1), and that the

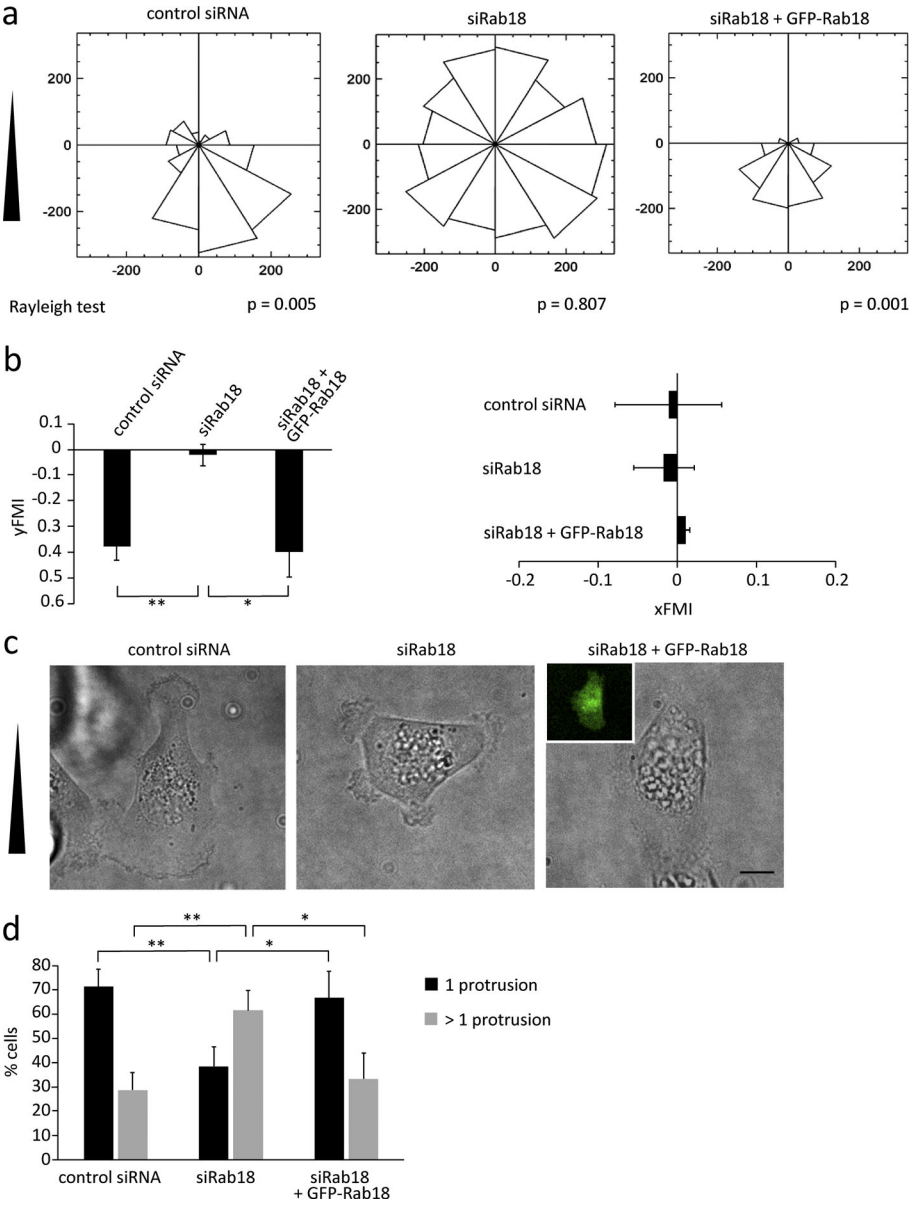

Figure 8. **Rab18 contributes to directional bias of cell migration during chemotaxis. (a)** Chemotaxis of MDA-MB-231 cells treated with control siRNA, siRNA against Rab18, or silenced for Rab18 and then transfected with GFP-Rab18, toward FCS. Cells were imaged in a chemotaxis chamber at 10-min intervals over a 2-h period. Direction of the chemoattractant gradient is toward the bottom. Rose plots and Rayleigh test show that the migration of control but not Rab18 knockdown cells is directionally biased. A total of 163 control cells, 194 Rab18 knockdown cells, and 73 cells silenced for Rab18 and then transfected with GFP-Rab18 from three independent experiments were quantified. **(b)** Quantification of the forward migration index in the x- and y-direction for the same cells as in panel a. *, P < 0.05; **, P < 0.01. **(c)** Transmission images of MDA-MB-231 cells treated with control siRNA, siRNA against Rab18, or silenced for Rab18 and then transfected with GFP-Rab18 (GFP channel in the inset) during chemotaxis. The direction of the chemoattractant gradient is toward the bottom. Scale bar: 10 µm. **(d)** Percentage of cells having one protrusion oriented toward the chemoattractant or multiple (>1) randomly oriented protrusions. The graph represents the mean ± SEM from three independent experiments (n > 50). *, P < 0.05; **, P < 0.01.

binding of both Rab18 and kinesin-1 to KNT1 is required for proper anterograde transport of the ER to establish contacts with FAs. Indeed, neither KNT1 TM mutant, which contains the Rab18-binding domain but lacks the kinesin-1–binding domain, nor KNT1 Δ201–445, which contains the kinesin-1–binding domain but lacks the Rab18-binding domain, rescued the defective ER–FA contacts in KNT1 knockdown cells (Fig. 3, c and d). Only the expression of KNT1 containing both the Rab18- and kinesin-1–binding sites (KNT1 FL) restored the formation of contacts between ER and FAs, further supporting that the KNT1-dependent transport of the ER toward the cell periphery is dependent on the binding to both Rab18 and kinesin-1.

Our results are consistent with a model in which KNT1 functions as an adaptor, bridging Rab18 to kinesin-1. Moreover, as depletion of Rab18 does not alter the binding of KIF5B to KNT1 (Fig. S1 b), but this binding is not sufficient to restore the defects in ER–FA contacts, it is the recruitment of active Rab18 to KNT1 that promotes the kinesin-1–mediated transport of the ER toward the cell periphery. Consistent with this, KNT1 accumulates in the perinuclear area in cells silenced for Rab18, resulting in a decreased localization to ER tubules (Fig. 2) and in a reduction in ER–FA contact points (Fig. 3, a and b), phenotypes reproduced by the KNT1 Δ201–445 mutant. This indicates that the binding of Rab18 is required for the correct localization and anterograde transport of KNT1 along microtubules to promote the formation of ER–FA contacts and FA growth.

In line with this, we found that Rab18 silencing decreases the size of FAs (Fig. 4, a and b) by altering their turnover (Fig. 6). Evidence on FA dynamics in invasive and noninvasive cell types shows that an increase in the FA disassembly rate is generally associated with an increase in cell invasion typical of metastatic cells. However, this occurs without alterations in the FA assembly rate (Bijian et al., 2013). As we measured an alteration in both FA assembly and disassembly rates upon Rab18 depletion, we speculate that it is the lack of sustained FA growth observed in cells silenced for Rab18 that prevents proper cell spreading and directional migration. In line with this, FAs form but do not mature in cells knocked down for Rab18, owing to the impaired formation of contacts between ER and FAs (Figs. 3 and 7). Rab18 is indeed required for the recruitment of both β3-integrin and vinculin at FAs (Fig. 7), suggesting that their transport at FAs is Rab18 dependent.

Intriguingly, αvβ3 integrin heterodimers are localized to the plasma membrane, Rab4- and Rab11-positive endosomes, but also to the ER (Woods et al., 2004). This indicates that the Rab18-KNT1-KIF5B complex might be involved in the trafficking of the ER-localized fraction of β3-integrin to FAs along the microtubules. Indeed, ER extension to β3-integrin plaques is microtubule dependent and serves as a prerequisite for β3-integrin recruitment and consequent growth of plaques (Zhang et al., 2010). Alternatively, Rab18 could control β3-integrin traffic to FAs more indirectly, for example by influencing the formation of ER–endosome contact sites. These contact sites determine spatial and temporal regulation of endosomal fission, and alterations of the ER structure and dynamics impair the ER-dependent process of endosome fission (Rowland et al., 2014). By regulating the ER morphology (Gerondopoulos et al., 2014), Rab18 could possibly be involved in this process of endosomal fission and thus promote β3-integrin recycling to the plasma membrane.

In addition to revealing a novel role for Rab18 in FA dynamics and maturation, the interaction with KNT1 may also help to shed light on the previously reported role of Rab18 in ER morphology. In the absence of Rab18, the ER tubular network is disrupted, and ER sheets are expanded (Gerondopoulos et al., 2014). Therefore, the cause for the impaired localization of KNT1 in the ER tubular network might be the decrease of tubular structures caused by Rab18 itself. However, the precise events regulated by Rab18 in this process are poorly characterized, most likely because the Rab18 effectors involved are so far unknown. As KNT1 is also involved in ER extension and its depletion increases the ER sheet/tubule ratio (Santama et al., 2004; Shibata et al., 2010), the altered ER morphology upon Rab18 depletion could be rather a consequence of an impaired binding to KNT1 that in turn affects the kinesin-1–mediated anterograde transport of the ER.

Altogether, our findings support a model in which active Rab18 directly binds to KNT1 to promote the kinesin-1–mediated transport of the ER necessary for FA growth and maturation, which is in turn required to maintain cell protrusions oriented toward a chemoattractant during chemotaxis. Indeed, in cells knocked down for Rab18, cells fail to correctly orient toward the chemoattractant (Fig. 8), similar to what has been already shown for KNT1 (Ng et al., 2016). FA assembly is regulated by the activation of FAK, a kinase that is a key regulator of adhesion and motility (Hamadi et al., 2005; Webb et al., 2002). Upon activation, FAK phosphorylates paxillin, which in turn recruits vinculin at the FAs (Case et al., 2015; Pasapera et al., 2010). In agreement with a defect in FA maturation upon Rab18 depletion, we measured a decrease in FAK phosphorylation at Tyr-397 (Fig. 7, d–g), a critical site for FAK activation (Chen et al., 1996). FAK is not only a key regulator of cell migration and FA turnover, but is also involved in mechanosensing, and forces within adhesions can drive FAK activation (Plotnikov et al., 2012; Zhou et al., 2015). According to this, and to the finding that FAK downstream signaling pathway is essential for cells to exert high traction (Plotnikov et al., 2012; Zhou et al., 2015), the decrease in FAK Tyr-397 phosphorylation upon Rab18 silencing correlates with the lower traction forces exerted by those cells (Fig. S3, c and d). It is therefore likely that the formation of FA–ER contacts provides the tension required to stimulate FAK phosphorylation and recruitment of FA proteins to sustain FA maturation and maintenance of oriented protrusions.

The delay in the generation of traction forces on substrate upon Rab18 depletion, however, indicates that cells lacking Rab18 are able to eventually generate a traction force similar to that of control cells (Fig. S3, c and d), despite defective FA maturation. This is in agreement with fact that the traction forces required to move the cells forward are dependent on small nascent FAs rather than mature adhesions (Beningo et al., 2001). Indeed, small adhesions can exert significant traction forces, with a magnitude that does not correlate with the adhesion size (Tan et al., 2003). Therefore, the ability of cells lacking Rab18 to generate traction forces but with a delay might not be linked to the defective FA maturation but rather to a delay in nascent adhesions.

Our data are consistent with the observation that decreased phosphorylation of FAK generally associates with reduced cancer cell motility and invasiveness (Hamadi et al., 2005; Li et al., 2015; Mendoza et al., 2013; Stokes et al., 2011; Tamura et al., 1998), whereas high levels of Tyr-397 phosphorylation are found in invasive cancers (Gabarra-Niecko et al., 2003; Grisaru-Granovsky et al., 2005; Sulzmaier et al., 2014; Zhao and Guan, 2009). Intriguingly, it has been recently reported that Rab18 is highly expressed in gastric cancer tissues and that Rab18-targeting microRNA-145-5p suppresses cell migration in hepatocellular carcinoma, suggesting that this small GTPase could indeed act as an oncogene (Liu et al., 2016; Wang et al., 2019).

In conclusion, our work reveals that Rab18 is a positive regulator of directional migration by controlling FA dynamics. We further demonstrate that this occurs as Rab18 directly interacts with and regulates KNT1 in a complex with the motor protein kinesin-1, thus mediating the transport of the ER to the cell surface necessary for the growth of FAs.

Materials and methods

Cell culture

U2OS and MDA-MB-231 cells were grown in DMEM (Lonza, BioWhittaker) supplemented with 10% FCS, 2 mM L-glutamine, 100 U/ml penicillin, and 100 µg/ml streptomycin kept at 37°C and 5% CO_2. GFP-KNT1 FL, GFP-KNT1 K1, or GFP-KNT1 Δ201–445 U2OS stable cell lines were generated under the selection of 0.5 mg/ml G418, and GFP-positive cells were sorted using a FacsAria III flow cytometer.

Reagents, constructs, and antibodies

pEGFP-C1 was purchased from BD Biosciences, Clontech. pEGFP-C1 Rab18 WT, pEGFP-C1 Rab18 Q67L, pEGFP-C1 Rab18 S22N, pcDNA 3.1 HA-Rab18 WT, pEGFP-C1 KNT1 Δ201–445, pGEX-2T KNT1 201–445, pET-16b His Rab18-Q67L, and siRNA-resistant pEGFP-C1 Rab18 containing silent mutations (used in rescue experiments) were purchased from GenScript. ER-GFP was purchased from Invitrogen. dsRED2-ER-5 was a gift from Michael Davidson (Florida State University, Tallahassee, FL; Addgene plasmid 55836). RFP-vinculin was a kind gift from Harald Stenmark (Institute for Cancer Research, Oslo University Hospital, Oslo, Norway). pEGFP KIF5B, pEGFP KNT1 FL, pEGFP KNT1 K1, pEGFP KNT^+, pEGFP KNT^-, and pEGFP KNT1 TM were kindly provided by Hanry Yu (Mechanobiology Institute, National University of Singapore, Singapore; Ong et al., 2000; Santama et al., 2004), and Vinculin-GFP was from Michael Sheetz's laboratory (Mechanobiology Institute, National University of Singapore, Singapore). β3-Integrin-YFP was a gift from Jonathan Jones (School of Molecular Biosciences, Washington State University, Pullman, WA; Addgene plasmid 26653; Tsuruta et al., 2002). RFP-Rab18 was obtained by subcloning Rab18 into the pTagRFP plasmid that was cut with XhoI and BamHI.

Rhodamine-conjugated phalloidin was purchased from Invitrogen (R415, 1:200). Primary antibodies used were anti-Rab18 (Abcam, 1:200), anti-Rab18 for GFP-TRAP experiments (Sigma-Aldrich 1:200), anti-vinculin (Sigma-Aldrich, 1:150), anti-β tubulin (Sigma-Aldrich, 1:12,000), anti-GFP (Abcam, 1:1,000), anti-FAK and anti-pFAK (Tyr397; Cell Signaling Technology, 1:3,000). Anti-KIF5B (Abcam) was diluted to 1:1,000 for Western blot experiments and 1:100 for coIP experiments. Anti-KNT1 (Cell Signaling Technology) was used at dilution 1:2,000 for Western blot analysis, 1:50 for coIP experiments, and 1:150 for immunofluorescence analysis. Anti-CLIMP-63 produced in mouse (Sigma-Aldrich) or rabbit (Proteintech) was used at 1:200 dilution, anti-RTN3 (Santa Cruz) at 1:1,000 dilution, and anti-GST (Sigma-Aldrich) at 1:30,000 dilution.

For immunofluorescence experiments, Alexa Fluor secondary antibodies (Invitrogen) were used at dilution 1:200. Secondary antibodies conjugated to HRP (GE Healthcare) were diluted 1:5,000 for immunoblotting studies. For nuclear staining, Hoechst dye (Life Technologies) was used at 0.2 µg/ml, and DAPI (Sigma-Aldrich) at 0.1 µg/ml.

Transfection and RNA interference

U2OS cells were transiently transfected using Lipofectamine 2000 (Life Technologies) following the manufacturer's instructions. Cells were transfected at ∼70% confluence for 24 h before further execution of experiments. MDA-MB-231 cells and U2OS cells for experiments on KNT1 mutants were transfected by using Amaxa nucleofector 2b (Lonza). For each condition, 500,000 cells were transfected with 2 µg of DNA.

For RNAi experiments, cells were transfected with siRNA using Lipofectamine RNAiMAX Transfection Reagent (Life Technologies) according to the manufacturer's instructions. The cells were transfected 24 h after plating at ∼50% confluence or by reverse transfection and analyzed after 72 h.

Nontargeting control siRNA (sense sequence 5′-ACUUCGAGC GUGCAUGGCUTT-3′ and antisense 5′-AGCCAUGCACGCUCGAA GUTT-3′) was purchased from MWG-Biotech. siRNAs directed against Rab18 (siRab18_1, J-010824-05; siRab18, J-010824-06) and against KNT1 (siKNT1 J-010605-05) were purchased from Dharmacon.

CoIP

For coIP experiments, GFP-Trap_MA (Chromotek) was used according to the manufacturer's instructions. Briefly, cells were transfected with GFP-fusion proteins, lysed in lysis buffer (10 mM Tris-HCl, pH 7.5, 150 mM NaCl, 0.5 mM EDTA, and 0.1% NP-40) and incubated for 1 h at 4°C with magnetic agarose beads coupled to antibody against GFP for coIP. Total lysates and immunoprecipitated samples were subsequently loaded on SDS-PAGE gels and subjected to Western blotting analysis.

Protein purification and direct interaction experiments

GST, GST-KNT1 (residues 201–445), and His-tagged Rab18Q67L were expressed in *Escherichia coli* BL21 (DE3; Agilent Technologies) after induction with 0.5 mM IPTG for 4 h at 37°C. The bacteria were centrifuged at 3,000 *g* for 15 min, resuspended in 64 mM Tris HCl, pH 8.5, 8 mM $MgCl_2$, 20 mM β-mercaptoethanol, and 0.30 mM PMSF, and lysed by French press. Expressed His-Rab18Q67L was purified from the bacterial soluble fraction using nickel-nitrilotriacetic acid resin (Qiagen) in the presence of 50 mM Tris, pH 8.0, 500 mM NaCl, 5%

glycerol, 1% Triton X-100, 5 mM β-mercaptoethanol, 20 mM Imidazole, and 0.3 mM PMSF, according to the manufacturer's protocol. Expressed GST and GST-KNT1 (201–445) were purified from the bacterial soluble fraction using Glutathione Sepharose resin, according to the manufacturer's protocol (GE Healthcare).

For the direct interaction, His-Rab18Q67L was incubated with either GST or GST-KNT1 (201–445) in PBS with 3 mM $MgCl_2$ and 0.2 mM GTPγS for 1 h at 4°C. Glutathione Sepharose resin was added to pull down the GST-tagged proteins, and samples were subjected to SDS-PAGE and Western blotting.

Immunoblotting

U2OS cells were lysed in lysis buffer (125 mM K-acetate, 25 mM Hepes, 5 mM EGTA, and 2.5 mM Mg-acetate, pH 7.2) complemented with 0.5% NP-40, protease inhibitor cocktail, and DTT. Cell lysates were subjected to SDS-PAGE and blotted onto polyvinylidene fluoride membranes (Millipore). The membranes were incubated overnight at 4°C with primary antibodies diluted in 2% blotting grade nonfat dry milk (Bio-Rad), followed by 1-h incubation with secondary antibodies conjugated to HRP (GE Healthcare). Either the ECL Prime Western Blotting Detection (GE Healthcare) or the SuperSignal West Femto Maximum Sensitivity Substrate (Thermo Scientific) followed by imaging using a Kodak Image Station 4000R equipped with a charge-coupled device camera were used for chemiluminescence detection. Quantification of chemiluminescence intensity was performed by densitometric analysis with ImageQuant TL software (GE Healthcare).

Chemotaxis assay

MDA-MB-231 cells were detached with 0.02% EDTA, and ∼18,000 cells were resuspended in basal medium containing 2% FCS and seeded onto µ-slide chemotaxis chambers (Ibidi; 80326). The chambers were filled with culture medium according to the manufacturer's instructions, and the cells were allowed to attach for 2 h at 37°C and 5% CO_2. 100% FCS was then added to one chamber's reservoir to generate the chemotactic gradient. Cells migrating toward the chemoattractant were imaged using an Andor Dragonfly spinning-disk confocal microscope with a 60× Apo objective, NA 1.4, at 10-min intervals for 2 h. Cell trajectories over time were tracked with the Manual Tracking plugin in ImageJ software (National Institutes of Health) and analyzed using the Chemotaxis and Migration Tool.

Cell spreading assay

U2OS cells were plated onto fibronectin-coated coverslips (10 µg/ml) and incubated for 1 h at 37°C and 5% CO_2 before fixation and staining with rhodamine-conjugated phalloidin and Hoechst. Quantification of the cell area was done using Fiji/ImageJ analysis software.

Micropatterns

96-Well plates (CYTOO, 20-900-00) containing L-shaped micropatterns (1,100 µm^2) were coated with 20 µg/ml fibronectin (Sigma-Aldrich) for 30 min. 3 × 10^3 cells were seeded in each well and incubated for 3.5 h at 37°C and 5% CO_2, before fixation and staining with rhodamine-conjugated phalloidin, vinculin, and Hoechst.

The analysis of actin distribution was performed in ImageJ, by using the CYTOOL-IP macro Hypothenuse that measures rigidity/collapse of the cell membrane (Degot et al., 2010). The macro aligns thresholded images of empty L-micropatterns and of the micropatterned cells, generating two image stacks. The stacks from the empty L-micropatterns were used to determine the theoretical hypotenuse position, while the stacks from the micropatterned cells stained for actin were used to determine cell contour and distance from the hypotenuse. The difference in the areas between the theoretical hypotenuse and the actual cell border was then measured. Based on this quantification, the cells were considered "straight" when no differences in the areas between the theoretical hypotenuse and the actual cell border were detected, or "curved" when the area difference resulted in a positive value. The CYTOOL-IP Cell Reference macro was used to analyze the actin distribution of cells plated on L-shaped micropatterns. This macro allows the alignment and averaging of several micropatterned cells stained for actin, generating a color-coded frequency map for a normalized mean cell that provides a statistical representation of the actin intracellular distribution.

Immunofluorescence and live-cell microscopy

For immunofluorescence, cells were grown on glass coverslips, fixed with 3% PFA, quenched using 50 mM NH_4Cl, and permeabilized by using 0.25% saponin (Sigma-Aldrich) in PBS 1×. Cells were incubated with primary antibodies at room temperature for 20 min, washed in 0.25% saponin in PBS, incubated with secondary antibodies in the dark at room temperature for 20 min, washed again in 0.25% saponin in PBS, and mounted with Mowiol. Fixed cells were imaged with an Olympus FluoView 1000 IX81 confocal laser scanning microscope (inverted) using a 60× PlanApo NA 1.35 objective. For imaging of the ER–FA contact points, cells were imaged with a Zeiss LSM880 microscope using a 63× oil Plan Apo NA 1 objective.

For live-cell imaging, cells were seeded on MatTek glass-bottom dishes. Before imaging, the culture medium was replaced with phenol red–free DMEM. During imaging, the cells were kept at 37°C and 5% CO_2. For live-cell image acquisition in studies on FA dynamics, multiple positions were imaged every 20 min using an inverted Olympus FluoView 1000 IX81 confocal laser scanning microscope equipped with a 60× PlanApo NA 1.35 objective The dynamics of Rab18 and FAs were studied using an Andor Dragonfly spinning-disk confocal microscope with a 60× Apo objective, NA 1.4.

FRAP

For the live-cell FRAP experiments, imaging was performed at 37°C and 5% CO_2 on a Spin SR SoRa microscope (Olympus) spinning disk system, equipped with a 60×/1.3 silicon immersion objective (UPLSAPO), two Orca-Flash 4.0 cameras (Hamamatsu), and a cellFRAP unit. The 405-nm laser was used to bleach the Vinculin-GFP or β3-integrin-YFP for 50 ms. Images were acquired as fast as possible for the first 100 images, and after that, every second minute.

Data from FRAP were normalized, corrected for bleaching (Pelkmans et al., 2001), and fitted by nonlinear regression to a

function that assumes a single diffusion coefficient (Yguerabide et al., 1982):

$$F(t) = \frac{F(0) + F(\infty)(t/t_{1/2})}{1 + (t/t_{1/2})}.$$

The values for $F(0)$, $F(\infty)$, and $T_{1/2}$ were calculated using GraphPad Prism 8, and the MFs were calculated as described in Lippincott-Schwartz et al., 2001. The MF defines the fraction of fluorescent molecules that can diffuse into the bleached region during the time course of the experiment (Lippincott-Schwartz et al., 2001).

Image processing and analysis

Image processing and analysis were performed using ImageJ/Fiji software (National Institutes of Health) and MATLAB R2017A. To quantify the accumulation of KNT1 in the perinuclear region, control and silenced U2OS cells were treated and imaged under identical conditions and microscope settings. The analysis was performed with the method of English and Voeltz (2013). Briefly, Z-stack maximum-intensity projection images were created, and two thresholded images were generated, one representing the perinuclear KNT1 and the second representing the total KNT1 staining. Three 5-pixel-thick line segments were drawn for each cell on both the thresholded images, irradiating from different regions along the nuclear envelope to the cell periphery. The percentage of perinuclear KNT1 in each line segment was measured, dividing the area of perinuclear KNT1 by the total area of the line segment.

Similarly, to quantify the distribution of KNT1 in the ER sheets and tubules, Z-stack maximum-intensity projection images were created from images acquired under identical conditions and microscope settings, and a thresholded image for KNT1 was generated. For the quantification of KNT1 in the ER sheets, CLIMP-63 staining was used to define the area of ER sheets. Three 5-pixel-thick line segments were drawn for each cell on both the KNT1 channel and the KNT1 thresholded image, irradiating from different regions along the nuclear envelope and extending either to the ER sheets area or to the cell periphery to define the total KNT1 area. The percentage of KNT1 in the ER sheet area for each 5–pixel line was calculated as follows:

$$\frac{F_{\mathrm{KNT1}}(\text{in ER sheets}) * A_{\mathrm{KNT1}}(\text{in ER sheets})}{\text{total } F_{\mathrm{KNT1}} * \text{total } A_{\mathrm{KNT1}}},$$

where F indicates the mean fluorescence for KNT1 and A the area occupied by KNT1 within the thresholded image.

For the quantification of KNT1 distribution in ER tubules, RTN3 staining was used to define the area of ER tubules. Three 5-pixel-thick line segments were drawn for each cell on both the KNT1 channel and the KNT1 thresholded image, irradiating from the cell periphery and extending until reaching the ER sheets area or further to the nuclear envelope to define the total KNT1 area. The percentage of KNT1 in the ER tubule area for each 5-pixel line was calculated as follows:

$$\frac{F_{\mathrm{KNT1}}(\text{in ER tubules}) * A_{\mathrm{KNT1}}(\text{in ER tubules})}{\text{total } F_{\mathrm{KNT1}} * \text{total } A_{\mathrm{KNT1}}}.$$

For the analysis of the contact points between the ER and FAs, maximum-intensity projection images for each channel were subjected to thresholding. The obtained masks were multiplied by using the Image Calculator plugin in Fiji. This operation generated a binary image showing the overlapping areas between the two channels that correspond to the FAs in contact with the ER. The number of these overlapping areas was counted and compared with the total number of peripheral FAs.

To analyze FAK phosphorylation at FAs, images were acquired with identical microscope settings. For quantification, the vinculin channel was thresholded and used to define the area of the FAs. The obtained region was then used on the pFAK channel, and the mean fluorescence of pFAK was measured for each adhesion.

FA analysis

For the analysis of FA number and size in ImageJ, after background subtraction and Gaussian filtering, the images were subjected to threshold and particles were analyzed. For studies on FA turnover, cells were transfected with RFP-vinculin and imaged every 10 min for 40 min. The total fluorescence intensity for 10 adhesions per cell was quantified for each time frame. An increase in total fluorescence in time was defined as FA assembly, whereas a reduction in total fluorescence indicated FA disassembly. FA assembly and disassembly rates were calculated as percentage of FAs that assembled or disassembled per minute.

For quantification of the colocalization between Rab18 and FAs, individual regions of interest containing one FA were selected, and the total intensity was calculated for GFP-Rab18 WT and RFP vinculin in each time frame. For GFP-Rab18, the total intensity was calculated over an area around the focal adhesion that was 4 × 4 pixels bigger than the FA area. This allowed measurement of the fluorescent signal of GFP-Rab18 in the region surrounding the selected FA.

Polydimethylsiloxane (PDMS) micropillars

Glass-bottom dishes (35-mm, Ibidi) were treated with O_2 plasma cleaning for 5 min. PDMS was mixed 10:1 with the curing agent (Sylgard 184, Dow Corning) and placed in a vacuum chamber for 20 min for degassing. A drop of the PDMS mixture was then dripped onto the plasma-treated glass-bottom dish. A silicon master substrate (Ghassemi et al., 2012), diameter 0.8 µm, height 1.3 µm, and stiffness 53.5 nN/µm, was rinsed with isopropanol twice and dried with nitrogen gas. The dried silicon substrate was placed onto the PDMS mixture on the glass-bottom dish, with the patterned surface facing down. A weight (M10 nut, 0.1N) was placed on top of the silicon master, and the whole device was placed in the vacuum chamber for another 20 min for degassing. The device was then transferred to a 70°C oven for 3 h for curing. PDMS pillar substrates were coated for 1 h with 10 µg/ml fibronectin. After washing, 50,000 cells per condition were plated on the coated micropillars and incubated for 2 h at 37°C and 5% CO_2. Time-lapse imaging of cells on pillars was performed with bright-field microscopy using a Zeiss LSM880 microscope maintained at 37°C and 5% CO_2 and using a 63× oil Plan Apo objective with NA 1. The position of each pillar in each frame was determined using the particle-tracking plugin

in ImageJ PillarTracker. The image-processing pipeline detects spots in the first frame and then uses them as seeds to track them over time (Tinevez et al., 2017). Based on the physical characteristics of the pillars and their displacement from the original positions, traction forces applied by the cells on pillars were quantified. Because the deflection δ is directly related to contracted or stretched force F by Euler–Bernoulli beam theory (Yang et al., 2016), the deflecting forces on the pillar induced by the cell are related via

$$F = \frac{3\pi d^4 E}{64L^3}\delta,$$

where L is the length or height of pillar, d is the diameter of round-section pillar, and E is the PDMS Young's modulus. The pillars we used have a Young's modulus E of 100 kPa, a diameter of 500 nm, and a height of 800 nm. The deflection δ is the quantity observed by imaging: the centroid of the projection of each pillar top shifts relative to the ensemble of the pillars at rest (those that show no movement), and hence absolute forces per pillar can be directly derived. The traction forces were analyzed by integrating the forces of a set of pillars over an entire cell perpendicular to the trajectory of the cell migration. To find the migration vector, we segmented the outlines of the entire cell, calculated the centers of gravity of the projection, and low-pass filtered the data to get a noise-free estimate of the direction of migration. The orthogonal force is the cross product of the total force with the trajectory in each time step.

Statistical analysis

Unless stated otherwise, evaluation of statistical differences was done by two-tailed unpaired Student's t test using Excel software. In the figures, statistical significance is shown as *, $P < 0.05$; **, $P < 0.01$; and ***, $P < 0.001$.

Online supplemental material

Fig. S1 shows that KNT1 interacts with KIF5B also in the absence of Rab18, while Rab18 needs KNT1 to associate with KIF5B. Fig. S2 presents live-cell imaging experiments of cells knocked down for Rab18 spreading onto fibronectin and analysis of the formation of contact points between ER and FAs. Fig. S3 illustrates the different phenotypes observed for cells plated on micropatterns. It also shows the force applied on micropillars by control cells and cells silenced for Rab18. Fig. S4 presents live imaging analysis of the dynamics of Rab18 and vinculin at FAs. Video 1 shows the dynamics of Rab18 and vinculin at FAs in a representative cell and supports Fig. S4.

Acknowledgments

We acknowledge Frode M. Skjeldal and the NorMIC Oslo imaging platform (Department of Biosciences, University of Oslo), Catherine Anne Heyward, and Sathiaruby Sivaganesh for technical assistance. We thank Ole Landsverk for help with cell sorting and Marcella Orwick Rydmark for help with French Press for bacterial lysis.

The financial support of the Norwegian Cancer Society (grants 5760850 and 4604944), the Research Council of Norway (grant 239903), the Anders Jahres Fond til Vitenskapens Fremme, the S. G. Sønneland Foundation, and UNIFOR-FRIMED 2019 is gratefully acknowledged.

The authors declare no competing financial interests.

Author contributions: N.A. Guadagno, A. Margiotta, S.A. Bjørnestad, L.H. Haugen, and I. Kjos performed experiments and analyzed data. X. Xu and F. Margadant carried out micropillar data processing. X. Hu fabricated and assisted with micropillars. C. Progida supervised the project. N.A. Guadagno and C. Progida designed the experiments and wrote the manuscript with input from all authors. O. Bakke and C. Progida conducted funding acquisition.

Submitted: 5 September 2018
Revised: 17 July 2019
Accepted: 26 March 2020

References

Abe, E., S. Okawa, M. Sugawara, S. Watanabe, and I. Toyoshima. 2007. Identification of ER membrane targeting signal of kinectin. *Neurosci. Lett.* 413:238–240. https://doi.org/10.1016/j.neulet.2006.11.064

Balaban, N.Q., U.S. Schwarz, D. Riveline, P. Goichberg, G. Tzur, I. Sabanay, D. Mahalu, S. Safran, A. Bershadsky, L. Addadi, et al. 2001. Force and focal adhesion assembly: a close relationship studied using elastic micropatterned substrates. *Nat. Cell Biol.* 3:466–472. https://doi.org/10.1038/35074532

Bem, D., S. Yoshimura, R. Nunes-Bastos, F.C. Bond, M.A. Kurian, F. Rahman, M.T. Handley, Y. Hadzhiev, I. Masood, A.A. Straatman-Iwanowska, et al. 2011. Loss-of-function mutations in RAB18 cause Warburg micro syndrome. *Am. J. Hum. Genet.* 88:499–507. https://doi.org/10.1016/j.ajhg.2011.03.012

Beningo, K.A., M. Dembo, I. Kaverina, J.V. Small, and Y.L. Wang. 2001. Nascent focal adhesions are responsible for the generation of strong propulsive forces in migrating fibroblasts. *J. Cell Biol.* 153:881–888. https://doi.org/10.1083/jcb.153.4.881

Bershadsky, A.D., N.Q. Balaban, and B. Geiger. 2003. Adhesion-dependent cell mechanosensitivity. *Annu. Rev. Cell Dev. Biol.* 19:677–695. https://doi.org/10.1146/annurev.cellbio.19.111301.153011

Bijian, K., C. Lougheed, J. Su, B. Xu, H. Yu, J.H. Wu, K. Riccio, and M.A. Alaoui-Jamali. 2013. Targeting focal adhesion turnover in invasive breast cancer cells by the purine derivative reversine. *Br. J. Cancer.* 109:2810–2818. https://doi.org/10.1038/bjc.2013.675

Borg, M., O. Bakke, and C. Progida. 2014. A novel interaction between Rab7b and actomyosin reveals a dual role in intracellular transport and cell migration. *J. Cell Sci.* 127:4927–4939. https://doi.org/10.1242/jcs.155861

Bravo-Cordero, J.J., M. Cordani, S.F. Soriano, B. Díez, C. Muñoz-Agudo, M. Casanova-Acebes, C. Boullosa, M.C. Guadamillas, I. Ezkurdia, D. González-Pisano, et al. 2016. A novel high-content analysis tool reveals Rab8-driven cytoskeletal reorganization through Rho GTPases, calpain and MT1-MMP. *J. Cell Sci.* 129:1734–1749. https://doi.org/10.1242/jcs.174920

Bryant, D.M., A. Datta, A.E. Rodríguez-Fraticelli, J. Peränen, F. Martín-Belmonte, and K.E. Mostov. 2010. A molecular network for de novo generation of the apical surface and lumen. *Nat. Cell Biol.* 12:1035–1045. https://doi.org/10.1038/ncb2106

Carpanini, S.M., L. McKie, D. Thomson, A.K. Wright, S.L. Gordon, S.L. Roche, M.T. Handley, H. Morrison, D. Brownstein, T.M. Wishart, et al. 2014. A novel mouse model of Warburg Micro syndrome reveals roles for RAB18 in eye development and organisation of the neuronal cytoskeleton. *Dis. Model. Mech.* 7:711–722. https://doi.org/10.1242/dmm.015222

Case, L.B., M.A. Baird, G. Shtengel, S.L. Campbell, H.F. Hess, M.W. Davidson, and C.M. Waterman. 2015. Molecular mechanism of vinculin activation and nanoscale spatial organization in focal adhesions. *Nat. Cell Biol.* 17:880–892. https://doi.org/10.1038/ncb3180

Chen, H.-C., P.A. Appeddu, H. Isoda, and J.-L. Guan. 1996. Phosphorylation of tyrosine 397 in focal adhesion kinase is required for binding phosphatidylinositol 3-kinase. *J. Biol. Chem.* 271:26329–26334. https://doi.org/10.1074/jbc.271.42.26329

Chevallier, J., C. Koop, A. Srivastava, R.J. Petrie, N. Lamarche-Vane, and J.F. Presley. 2009. Rab35 regulates neurite outgrowth and cell shape. *FEBS Lett.* 583:1096–1101. https://doi.org/10.1016/j.febslet.2009.03.012

Degot, S., M. Auzan, V. Chapuis, A. Béghin, A. Chadeyras, C. Nelep, M.L. Calvo-Muñoz, J. Young, F. Chatelain, and A. Fuchs. 2010. Improved visualization and quantitative analysis of drug effects using micropatterned cells. *J. Vis. Exp.* (46):2514.

Dejgaard, S.Y., A. Murshid, A. Erman, O. Kizilay, D. Verbich, R. Lodge, K. Dejgaard, T.B.N. Ly-Hartig, R. Pepperkok, J.C. Simpson, et al. 2008. Rab18 and Rab43 have key roles in ER-Golgi trafficking. *J. Cell Sci.* 121: 2768–2781. https://doi.org/10.1242/jcs.021808

English, A.R., and G.K. Voeltz. 2013. Rab10 GTPase regulates ER dynamics and morphology. *Nat. Cell Biol.* 15:169–178. https://doi.org/10.1038/ncb2647

Fütterer, A., G. Kruppa, B. Krämer, H. Lemke, and M. Krönke. 1995. Molecular cloning and characterization of human kinectin. *Mol. Biol. Cell.* 6: 161–170. https://doi.org/10.1091/mbc.6.2.161

Gabarra-Niecko, V., M.D. Schaller, and J.M. Dunty. 2003. FAK regulates biological processes important for the pathogenesis of cancer. *Cancer Metastasis Rev.* 22:359–374. https://doi.org/10.1023/A:1023725029589

Gallwitz, D., C. Donath, and C. Sander. 1983. A yeast gene encoding a protein homologous to the human c-has/bas proto-oncogene product. *Nature.* 306:704–707. https://doi.org/10.1038/306704a0

Gerondopoulos, A., R.N. Bastos, S. Yoshimura, R. Anderson, S. Carpanini, I. Aligianis, M.T. Handley, and F.A. Barr. 2014. Rab18 and a Rab18 GEF complex are required for normal ER structure. *J. Cell Biol.* 205:707–720. https://doi.org/10.1083/jcb.201403026

Ghassemi, S., G. Meacci, S. Liu, A.A. Gondarenko, A. Mathur, P. Roca-Cusachs, M.P. Sheetz, and J. Hone. 2012. Cells test substrate rigidity by local contractions on submicrometer pillars. *Proc. Natl. Acad. Sci. USA.* 109:5328–5333. https://doi.org/10.1073/pnas.1119886109

Gibieža, P., and R. Prekeris. 2018. Rab GTPases and cell division. *Small GTPases.* 9:107–115.

Gillingham, A.K., R. Sinka, I.L. Torres, K.S. Lilley, and S. Munro. 2014. Toward a comprehensive map of the effectors of rab GTPases. *Dev. Cell.* 31: 358–373. https://doi.org/10.1016/j.devcel.2014.10.007

Grisaru-Granovsky, S., Z. Salah, M. Maoz, D. Pruss, U. Beller, and R. Bar-Shavit. 2005. Differential expression of protease activated receptor 1 (Par1) and pY397FAK in benign and malignant human ovarian tissue samples. *Int. J. Cancer.* 113:372–378. https://doi.org/10.1002/ijc.20607

Hamadi, A., M. Bouali, M. Dontenwill, H. Stoeckel, K. Takeda, and P. Rondé. 2005. Regulation of focal adhesion dynamics and disassembly by phosphorylation of FAK at tyrosine 397. *J. Cell Sci.* 118:4415–4425. https://doi.org/10.1242/jcs.02565

Humphries, J.D., P. Wang, C. Streuli, B. Geiger, M.J. Humphries, and C. Ballestrem. 2007. Vinculin controls focal adhesion formation by direct interactions with talin and actin. *J. Cell Biol.* 179:1043–1057. https://doi.org/10.1083/jcb.200703036

Jayson, C.B.K., H. Arlt, A.W. Fischer, Z.W. Lai, R.V. Farese, T.C. Walther, and F.A. Barr. 2018. Rab18 is not necessary for lipid droplet biogenesis or turnover in human mammary carcinoma cells. *Mol. Biol. Cell.* 29:2045–2054.

Jian, Q., Y. Miao, L. Tang, M. Huang, Y. Yang, W. Ba, Y. Liu, S. Chi, and C. Li. 2016. Rab23 promotes squamous cell carcinoma cell migration and invasion via integrin β1/Rac1 pathway. *Oncotarget.* 7:5342–5352. https://doi.org/10.18632/oncotarget.6701

Kjos, I., K. Vestre, N.A. Guadagno, M. Borg Distefano, and C. Progida. 2018. Rab and Arf proteins at the crossroad between membrane transport and cytoskeleton dynamics. *Biochim. Biophys. Acta Mol. Cell Res.* 1865:1397–1409. https://doi.org/10.1016/j.bbamcr.2018.07.009

Klöpper, T.H., N. Kienle, D. Fasshauer, and S. Munro. 2012. Untangling the evolution of Rab G proteins: implications of a comprehensive genomic analysis. *BMC Biol.* 10:71. https://doi.org/10.1186/1741-7007-10-71

Kouranti, I., M. Sachse, N. Arouche, B. Goud, and A. Echard. 2006. Rab35 regulates an endocytic recycling pathway essential for the terminal steps of cytokinesis. *Curr. Biol.* 16:1719–1725. https://doi.org/10.1016/j.cub.2006.07.020

Kumar, J., H. Yu, and M.P. Sheetz. 1995. Kinectin, an essential anchor for kinesin-driven vesicle motility. *Science.* 267:1834–1837. https://doi.org/10.1126/science.7892610

Lanzetti, L., A. Palamidessi, L. Areces, G. Scita, and P.P. Di Fiore. 2004. Rab5 is a signalling GTPase involved in actin remodelling by receptor tyrosine kinases. *Nature.* 429:309–314. https://doi.org/10.1038/nature02542

Li, D., Y.G. Zhao, D. Li, H. Zhao, J. Huang, G. Miao, D. Feng, P. Liu, D. Li, and H. Zhang. 2019. The ER-Localized Protein DFCP1 Modulates ER-Lipid Droplet Contact Formation. *Cell Rep.* 27:343–358.e5. https://doi.org/10.1016/j.celrep.2019.03.025

Li, W.-X., L.-P. Chen, M.-Y. Sun, J.-T. Li, H.-Z. Liu, and W. Zhu. 2015. 3′3-Diindolylmethane inhibits migration, invasion and metastasis of hepatocellular carcinoma by suppressing FAK signaling. *Oncotarget.* 6: 23776–23792. https://doi.org/10.18632/oncotarget.4196

Linford, A., S. Yoshimura, R. Nunes Bastos, L. Langemeyer, A. Gerondopoulos, D.J. Rigden, and F.A. Barr. 2012. Rab14 and its exchange factor FAM116 link endocytic recycling and adherens junction stability in migrating cells. *Dev. Cell.* 22:952–966. https://doi.org/10.1016/j.devcel.2012.04.010

Lippincott-Schwartz, J., E. Snapp, and A. Kenworthy. 2001. Studying protein dynamics in living cells. *Nat. Rev. Mol. Cell Biol.* 2:444–456. https://doi.org/10.1038/35073068

Liu, J., J. Zhang, Y. Li, L. Wang, B. Sui, and D. Dai. 2016. MiR-455-5p acts as a novel tumor suppressor in gastric cancer by down-regulating RAB18. *Gene.* 592:308–315. https://doi.org/10.1016/j.gene.2016.07.034

Livne, A., and B. Geiger. 2016. The inner workings of stress fibers - from contractile machinery to focal adhesions and back. *J. Cell Sci.* 129: 1293–1304. https://doi.org/10.1242/jcs.180927

Margiotta, A., C. Progida, O. Bakke, and C. Bucci. 2017. Rab7a regulates cell migration through Rac1 and vimentin. *Biochim. Biophys. Acta Mol. Cell Res.* 1864:367–381. https://doi.org/10.1016/j.bbamcr.2016.11.020

Martin, S., K. Driessen, S.J. Nixon, M. Zerial, and R.G. Parton. 2005. Regulated localization of Rab18 to lipid droplets: effects of lipolytic stimulation and inhibition of lipid droplet catabolism. *J. Biol. Chem.* 280: 42325–42335. https://doi.org/10.1074/jbc.M506651200

Mendoza, P., R. Ortiz, J. Díaz, A.F.G. Quest, L. Leyton, D. Stupack, and V.A. Torres. 2013. Rab5 activation promotes focal adhesion disassembly, migration and invasiveness in tumor cells. *J. Cell Sci.* 126:3835–3847. https://doi.org/10.1242/jcs.119727

Mitra, S.K., and D.D. Schlaepfer. 2006. Integrin-regulated FAK-Src signaling in normal and cancer cells. *Curr. Opin. Cell Biol.* 18:516–523. https://doi.org/10.1016/j.ceb.2006.08.011

Ng, I.C., P. Pawijit, L.Y. Teo, H. Li, S.Y. Lee, and H. Yu. 2016. Kinectin-dependent ER transport supports the focal complex maturation required for chemotaxis in shallow gradients. *J. Cell Sci.* 129:2660–2672. https://doi.org/10.1242/jcs.181768

Ong, L.-L., A.P.C. Lim, C.P.N. Er, S.A. Kuznetsov, and H. Yu. 2000. Kinectin-kinesin binding domains and their effects on organelle motility. *J. Biol. Chem.* 275:32854–32860. https://doi.org/10.1074/jbc.M005650200

Ozeki, S., J. Cheng, K. Tauchi-Sato, N. Hatano, H. Taniguchi, and T. Fujimoto. 2005. Rab18 localizes to lipid droplets and induces their close apposition to the endoplasmic reticulum-derived membrane. *J. Cell Sci.* 118: 2601–2611. https://doi.org/10.1242/jcs.02401

Palamidessi, A., E. Frittoli, M. Garré, M. Faretta, M. Mione, I. Testa, A. Diaspro, L. Lanzetti, G. Scita, and P.P. Di Fiore. 2008. Endocytic trafficking of Rac is required for the spatial restriction of signaling in cell migration. *Cell.* 134:135–147. https://doi.org/10.1016/j.cell.2008.05.034

Pasapera, A.M., I.C. Schneider, E. Rericha, D.D. Schlaepfer, and C.M. Waterman. 2010. Myosin II activity regulates vinculin recruitment to focal adhesions through FAK-mediated paxillin phosphorylation. *J. Cell Biol.* 188:877–890. https://doi.org/10.1083/jcb.200906012

Pelkmans, L., J. Kartenbeck, and A. Helenius. 2001. Caveolar endocytosis of simian virus 40 reveals a new two-step vesicular-transport pathway to the ER. *Nat. Cell Biol.* 3:473–483. https://doi.org/10.1038/35074539

Plotnikov, S.V., A.M. Pasapera, B. Sabass, and C.M. Waterman. 2012. Force fluctuations within focal adhesions mediate ECM-rigidity sensing to guide directed cell migration. *Cell.* 151:1513–1527. https://doi.org/10.1016/j.cell.2012.11.034

Rowland, A.A., P.J. Chitwood, M.J. Phillips, and G.K. Voeltz. 2014. ER contact sites define the position and timing of endosome fission. *Cell.* 159: 1027–1041. https://doi.org/10.1016/j.cell.2014.10.023

Santama, N., C.P.N. Er, L.-L. Ong, and H. Yu. 2004. Distribution and functions of kinectin isoforms. *J. Cell Sci.* 117:4537–4549. https://doi.org/10.1242/jcs.01326

Schmitt, H.D., P. Wagner, E. Pfaff, and D. Gallwitz. 1986. The ras-related YPT1 gene product in yeast: a GTP-binding protein that might be involved in microtubule organization. *Cell.* 47:401–412. https://doi.org/10.1016/0092-8674(86)90597-0

Schoen, I., W. Hu, E. Klotzsch, and V. Vogel. 2010. Probing cellular traction forces by micropillar arrays: contribution of substrate warping to pillar deflection. *Nano Lett.* 10:1823–1830. https://doi.org/10.1021/nl100533c

Shi, Q., and D. Boettiger. 2003. A novel mode for integrin-mediated signaling: tethering is required for phosphorylation of FAK Y397. *Mol. Biol. Cell.* 14: 4306–4315. https://doi.org/10.1091/mbc.e03-01-0046

Shibata, Y., T. Shemesh, W.A. Prinz, A.F. Palazzo, M.M. Kozlov, and T.A. Rapoport. 2010. Mechanisms determining the morphology of the peripheral ER. *Cell.* 143:774–788. https://doi.org/10.1016/j.cell.2010.11.007

Stokes, J.B., S.J. Adair, J.K. Slack-Davis, D.M. Walters, R.W. Tilghman, E.D. Hershey, B. Lowrey, K.S. Thomas, A.H. Bouton, R.F. Hwang, et al. 2011. Inhibition of focal adhesion kinase by PF-562,271 inhibits the growth and metastasis of pancreatic cancer concomitant with altering the tumor microenvironment. *Mol. Cancer Ther*. 10:2135–2145. https://doi.org/10.1158/1535-7163.MCT-11-0261

Sulzmaier, F.J., C. Jean, and D.D. Schlaepfer. 2014. FAK in cancer: mechanistic findings and clinical applications. *Nat. Rev. Cancer*. 14:598–610. https://doi.org/10.1038/nrc3792

Sun, Z., S.S. Guo, and R. Fässler. 2016. Integrin-mediated mechanotransduction. *J. Cell Biol*. 215:445–456. https://doi.org/10.1083/jcb.201609037

Tamura, M., J. Gu, K. Matsumoto, S. Aota, R. Parsons, and K.M. Yamada. 1998. Inhibition of cell migration, spreading, and focal adhesions by tumor suppressor PTEN. *Science*. 280:1614–1617. https://doi.org/10.1126/science.280.5369.1614

Tan, J.L., J. Tien, D.M. Pirone, D.S. Gray, K. Bhadriraju, and C.S. Chen. 2003. Cells lying on a bed of microneedles: an approach to isolate mechanical force. *Proc. Natl. Acad. Sci. USA*. 100:1484–1489. https://doi.org/10.1073/pnas.0235407100

Théry, M.. 2010. Micropatterning as a tool to decipher cell morphogenesis and functions. *J. Cell Sci*. 123:4201–4213. https://doi.org/10.1242/jcs.075150

Thomas, J.D., Y.J. Zhang, Y.H. Wei, J.H. Cho, L.E. Morris, H.Y. Wang, and X.F. Zheng. 2014. Rab1A is an mTORC1 activator and a colorectal oncogene. *Cancer Cell*. 26:754–769. https://doi.org/10.1016/j.ccell.2014.09.008

Tinevez, J.-Y., N. Perry, J. Schindelin, G.M. Hoopes, G.D. Reynolds, E. Laplantine, S.Y. Bednarek, S.L. Shorte, and K.W. Eliceiri. 2017. TrackMate: An open and extensible platform for single-particle tracking. *Methods*. 115:80–90. https://doi.org/10.1016/j.ymeth.2016.09.016

Toyoshima, I., H. Yu, E.R. Steuer, and M.P. Sheetz. 1992. Kinectin, a major kinesin-binding protein on ER. *J. Cell Biol*. 118:1121–1131. https://doi.org/10.1083/jcb.118.5.1121

Tsuruta, D., M. Gonzales, S.B. Hopkinson, C. Otey, S. Khuon, R.D. Goldman, and J.C. Jones. 2002. Microfilament-dependent movement of the beta3 integrin subunit within focal contacts of endothelial cells. *FASEB J*. 16:866–868. https://doi.org/10.1096/fj.01-0878fje

Vazquez-Martinez, R., D. Cruz-Garcia, M. Duran-Prado, J.R. Peinado, J.P. Castaño, and M.M. Malagon. 2007. Rab18 inhibits secretory activity in neuroendocrine cells by interacting with secretory granules. *Traffic*. 8:867–882. https://doi.org/10.1111/j.1600-0854.2007.00570.x

Vestre, K., I. Kjos, N.A. Guadagno, M. Borg Distefano, F. Kohler, F. Fenaroli, O. Bakke, and C. Progida. 2019. Rab6 regulates cell migration and invasion by recruiting Cdc42 and modulating its activity. *Cell. Mol. Life Sci*. 76:2593–2614. https://doi.org/10.1007/s00018-019-03057-w

Wandinger-Ness, A., and M. Zerial. 2014. Rab proteins and the compartmentalization of the endosomal system. *Cold Spring Harb. Perspect. Biol*. 6. a022616. https://doi.org/10.1101/cshperspect.a022616

Wang, B., W. Dong, and X. Li. 2019. miR-145-5p Acts as a Novel Tumor Suppressor in Hepatocellular Carcinoma Through Targeting RAB18. *Technol. Cancer Res. Treat*. 18. 1533033819850189. https://doi.org/10.1177/1533033819850189

Webb, D.J., K. Donais, L.A. Whitmore, S.M. Thomas, C.E. Turner, J.T. Parsons, and A.F. Horwitz. 2004. FAK-Src signalling through paxillin, ERK and MLCK regulates adhesion disassembly. *Nat. Cell Biol*. 6:154–161. https://doi.org/10.1038/ncb1094

Webb, D.J., J.T. Parsons, and A.F. Horwitz. 2002. Adhesion assembly, disassembly and turnover in migrating cells -- over and over and over again. *Nat. Cell Biol*. 4:E97–E100. https://doi.org/10.1038/ncb0402-e97

Woods, A.J., D.P. White, P.T. Caswell, and J.C. Norman. 2004. PKD1/PKCmu promotes alphavbeta3 integrin recycling and delivery to nascent focal adhesions. *EMBO J*. 23:2531–2543. https://doi.org/10.1038/sj.emboj.7600267

Wu, Q., X. Sun, W. Yue, T. Lu, Y. Ruan, T. Chen, and D. Zhang. 2016. RAB18, a protein associated with Warburg Micro syndrome, controls neuronal migration in the developing cerebral cortex. *Mol. Brain*. 9:19. https://doi.org/10.1186/s13041-016-0198-2

Xu, D., Y. Li, L. Wu, Y. Li, D. Zhao, J. Yu, T. Huang, C. Ferguson, R.G. Parton, H. Yang, et al. 2018. Rab18 promotes lipid droplet (LD) growth by tethering the ER to LDs through SNARE and NRZ interactions. *J. Cell Biol*. 217:975–995. https://doi.org/10.1083/jcb.201704184

Yang, B., Z.Z. Lieu, H. Wolfenson, F.M. Hameed, A.D. Bershadsky, and M.P. Sheetz. 2016. Mechanosensing Controlled Directly by Tyrosine Kinases. *Nano Lett*. 16:5951–5961. https://doi.org/10.1021/acs.nanolett.6b02995

Yguerabide, J., J.A. Schmidt, and E.E. Yguerabide. 1982. Lateral mobility in membranes as detected by fluorescence recovery after photobleaching. *Biophys. J*. 40:69–75. https://doi.org/10.1016/S0006-3495(82)84459-7

Yu, H., C.V. Nicchitta, J. Kumar, M. Becker, I. Toyoshima, and M.P. Sheetz. 1995. Characterization of kinectin, a kinesin-binding protein: primary sequence and N-terminal topogenic signal analysis. *Mol. Biol. Cell*. 6:171–183. https://doi.org/10.1091/mbc.6.2.171

Zaidel-Bar, R., C. Ballestrem, Z. Kam, and B. Geiger. 2003. Early molecular events in the assembly of matrix adhesions at the leading edge of migrating cells. *J. Cell Sci*. 116:4605–4613. https://doi.org/10.1242/jcs.00792

Zhang, X., Y.H. Tee, J.K. Heng, Y. Zhu, X. Hu, F. Margadant, C. Ballestrem, A. Bershadsky, G. Griffiths, and H. Yu. 2010. Kinectin-mediated endoplasmic reticulum dynamics supports focal adhesion growth in the cellular lamella. *J. Cell Sci*. 123:3901–3912. https://doi.org/10.1242/jcs.069153

Zhao, J., and J.-L. Guan. 2009. Signal transduction by focal adhesion kinase in cancer. *Cancer Metastasis Rev*. 28:35–49. https://doi.org/10.1007/s10555-008-9165-4

Zhen, Y., and H. Stenmark. 2015. Cellular functions of Rab GTPases at a glance. *J. Cell Sci*. 128:3171–3176. https://doi.org/10.1242/jcs.166074

Zhou, J., C. Aponte-Santamaría, S. Sturm, J.T. Bullerjahn, A. Bronowska, and F. Gräter. 2015. Mechanism of Focal Adhesion Kinase Mechanosensing. *PLOS Comput. Biol*. 11. e1004593. https://doi.org/10.1371/journal.pcbi.1004593

Supplemental material

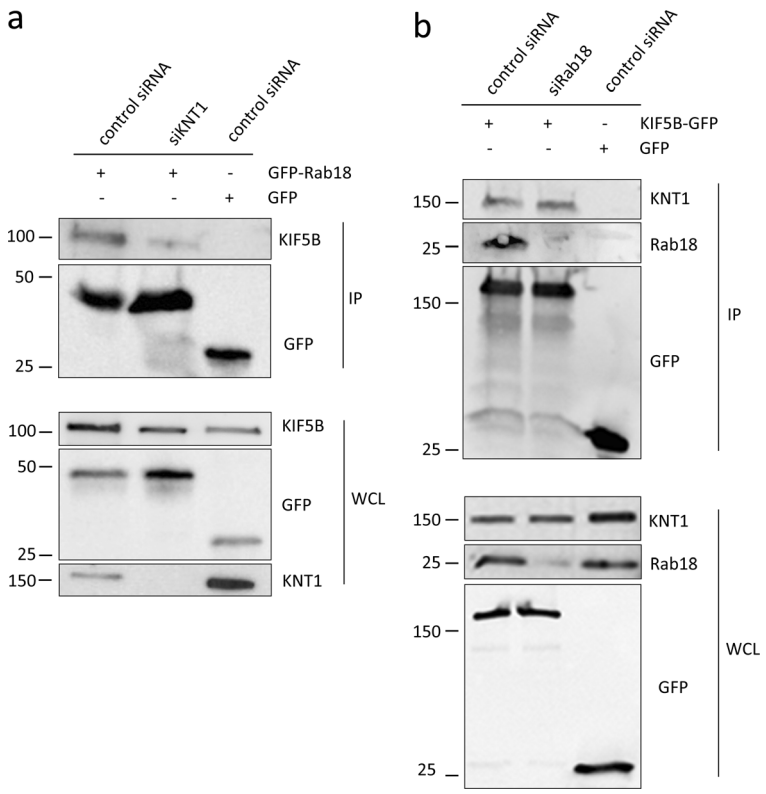

Figure S1. **KNT1 is an adaptor that connects Rab18 to KIF5B. (a)** U2OS cells treated with either control siRNA or siRNA directed against KNT1, and transfected with either GFP or GFP-Rab18, were lysed and immunoprecipitated with GFP magnetic agarose beads. Whole-cell lysates (WCL) and immunoprecipitates (IP) were subjected to Western blot analysis using the indicated antibodies. **(b)** U2OS cells treated with either control siRNA or siRNA directed against Rab18, and transfected with either GFP or KIF5B-GFP, were lysed and immunoprecipitated with GFP magnetic agarose beads. WCL and IP were subjected to Western blot analysis using the indicated antibodies.

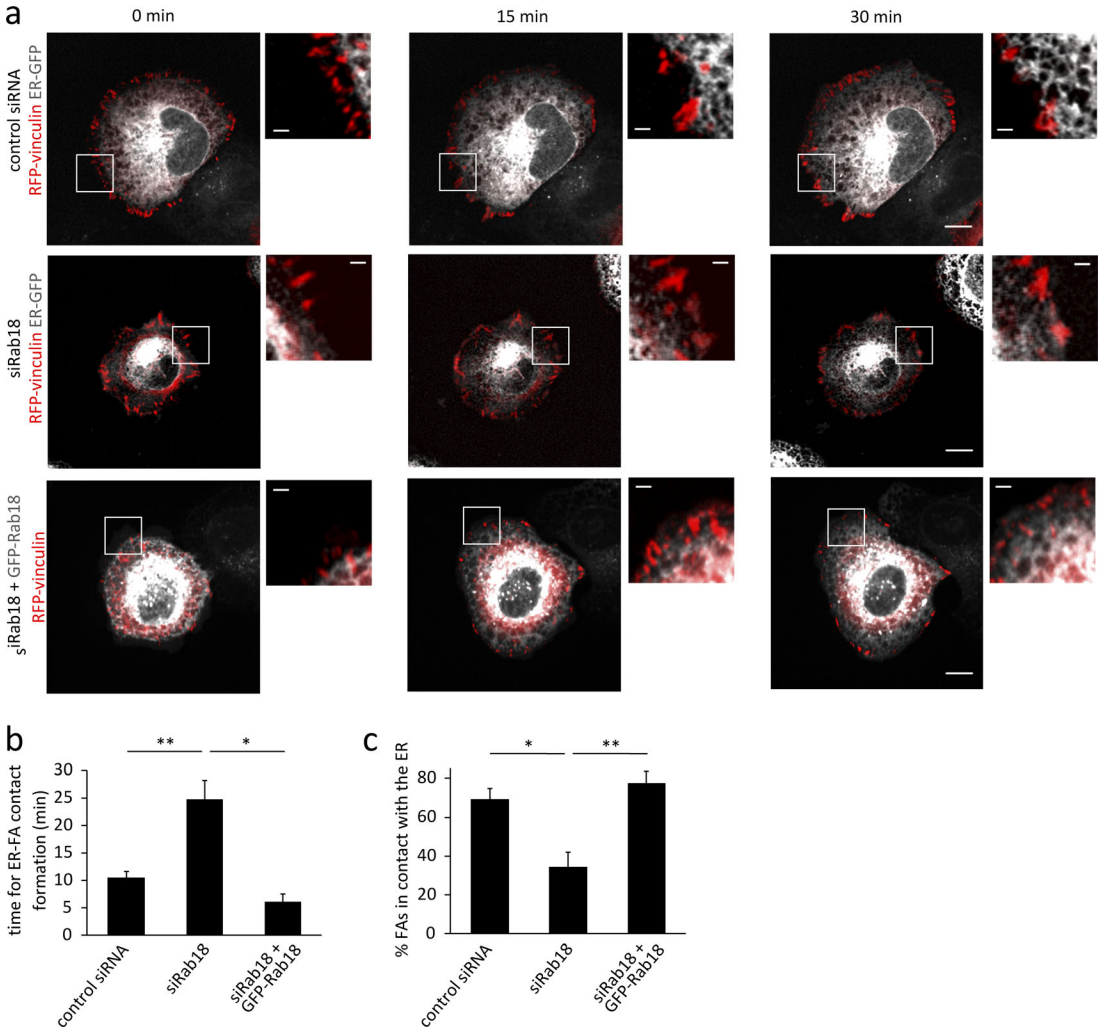

Figure S2. **Knockdown of Rab18 delays the formation of ER–FA contacts. (a)** Live imaging of U2OS cells treated with control siRNA or siRab18 and transfected with with RFP-vinculin and either ER-GFP or GFP-Rab18 as indicated. Cells were plated on fibronectin-coated dishes and imaged every 15 min with a spinning disk confocal microscope. Scale bar: 10 µm; insets: 2 µm. **(b)** Quantification of the time required for the formation of ER–FA contacts. The graph represents the mean ± SEM for at least three experiments (n > 20). *, P < 0.05; **, P < 0.01. **(c)** Quantification of the percentage of FAs in contact with the ER. The graph represents the mean ± SEM for at least three experiments (n > 20). *, P < 0.05; **, P < 0.01.

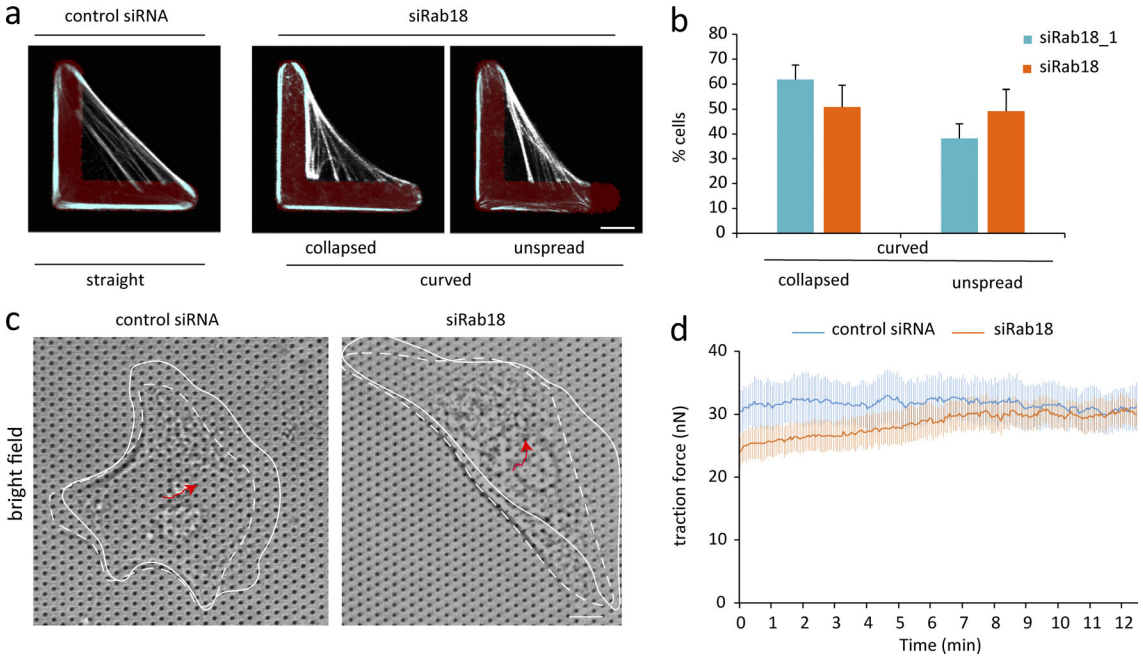

Figure S3. **Rab18 depletion affects stress fibers formation on L-shaped micropattern and traction force generation. (a)** U2OS cells were plated onto fibronectin-coated L-shaped micropatterns and left to adhere for 3.5 h before fixation and staining with rhodamine-conjugated phalloidin. The images illustrate examples of cells on micropatterns with "straight" or "curved" hypotenuse. The curved phenotype includes both cells with the collapsed hypotenuse (collapsed) or partially spread (unspread). Scale bar: 10 µm. **(b)** The graph shows the percentage of collapsed or unspread cells in samples silenced for Rab18 using siRNA Rab18 or siRNA Rab18_1 (mean ± SEM). *n* > 80 cells from three independent experiments. **(c)** U2OS cells transfected with siRNA control or siRNA Rab18 were plated on fibronectin-coated micropillars and imaged over time. The white lines indicate the cell borders at T_0 (dotted line) and after 12 min (solid line). Red arrows indicates the cell trajectory. Scale bar: 5 µm. **(d)** Quantification of the traction forces within the cells. The graph represents the mean ± SEM of *n* > 20 cells from three independent experiments. A pairwise *t* test ($P < 0.001$) was performed with Mathematica software. The nonparametric rank test (Wilcoxon media test) was also significant ($P < 0.001$).

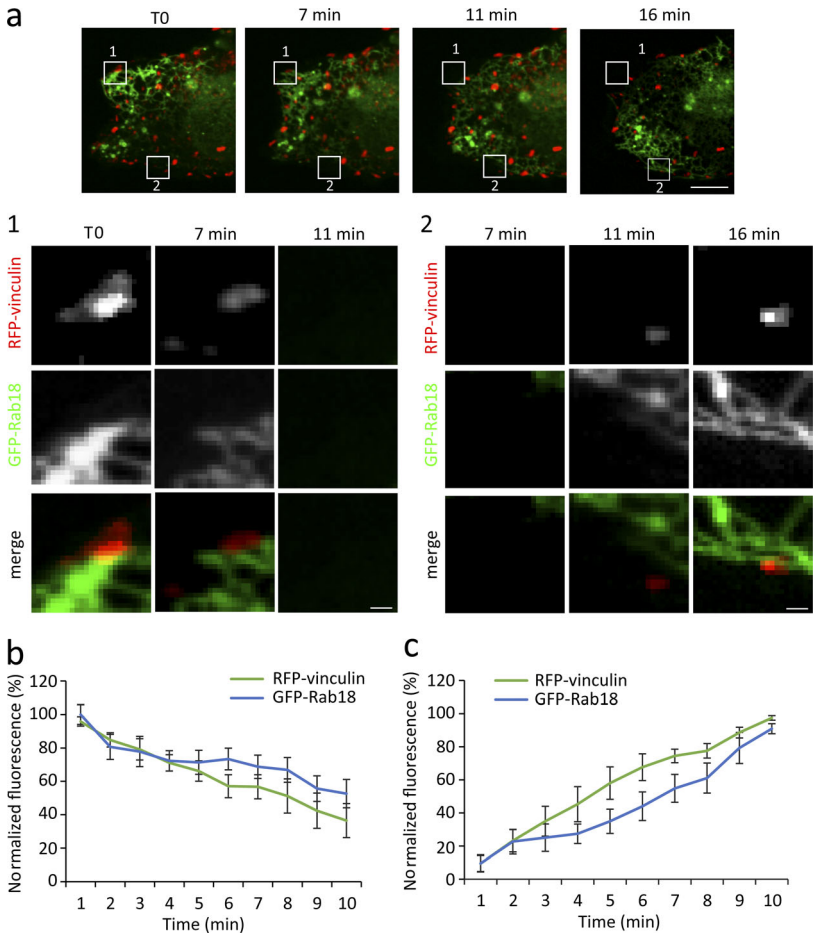

Figure S4. **Live dynamics of FA assembly and disassembly together with Rab18. (a)** Live-cell imaging of U2OS cells cotransfected with GFP-Rab18 and RFP-vinculin. Cells were imaged every minute with a spinning disk confocal microscope. Magnifications of the boxed areas are shown in the lower panels and illustrate an example of FA disassembly (1) or assembly (2). Scale bars: top, 10 µm; bottom, 1 µm. **(b and c)** Fluorescence intensity profiles over time for GFP-Rab18 and RFP-vinculin at FAs. Fluorescence intensity profiles were individually normalized between 0 and 100 and then averaged. The graphs represent the mean intensity profiles ± SEM from four independent live-cell imaging experiments (n = 10).

Video 1. **Live-cell imaging of U2OS cells cotransfected with GFP-Rab18 (green) and RFP-vinculin (red).** Cells were imaged every minute with a spinning disk confocal microscope. Magnifications of the boxed areas are shown in the side panels and illustrate an example of FA disassembly (1) or assembly (2).